Supporting information

Catalytic Ammonia Synthesis on HY Zeolite-Supported Angstrom-size Molybdenum Cluster

Satoshi Kamiguchi, Kiyotaka Asakura, Tamaki Shibayama, Tomoko Yokaichiya, Tatsushi Ikeda, Akira Nakayama,* Ken-ichi Shimizu, Zhaomin Hou*

Table of Contents

Experimental Methods

General procedure

For all gas-flow experiments, extra-pure H_2 (>99.99999 vol.%), N_2 (>99.99995 vol.%), Ar (>99.9999 vol.%), and mixture of N_2/H_2 (25% vol.%, O_2 impurity < 0.00001 vol.%, H_2O impurity < 0.00005 vol.%) were used. Oxygen- and moisture-sensitive samples were handled under a dry and oxygen-free Ar atmosphere in an Mbraun glovebox. The Ar was constantly circulated through a copper/molecular sieves catalyst unit. The oxygen and moisture concentrations in the glovebox atmosphere were monitored by an O_2/H_2O Combi-Analyzer (Mbraun) to ensure both were always below 0.1 ppm.

Preparation of supported molybdenum cluster catalyst precursor

A molecular hexanuclear cluster complex $(H_3O)_2[(Mo_6Cl_8)Cl_6]\cdot 6H_2O$ (**1**) was prepared according to published procedures.[1a] The resulting **1** was heated in vacuo to afford Mo_6Cl_{12}, followed by extraction with hot hydrochloric acid and recrystallization, before use.[1b] HY zeolite (HSZ-390HUA with a SiO_2/Al_2O_3 molar ratio of 810) and HZSM5 zeolite (HSZ-891HOA with a SiO_2/Al_2O_3 molar ration of 2120) were purchased from Tosoh Co. (These SiO_2/Al_2O_3 molar ratios were analyzed for the used samples before the purchase.) Mesoporous silica MCM-41 was purchased from Sigma-Aldrich. These supports were used as received. The supported Mo clusters were prepared using a conventional impregnation method. A methanol solution of **1** (8.3×10^{-4} wt%) was added to each support with a weight ratio of **1** and the support as 5:95 (2.36 wt% Mo), followed by stirring of the resulting suspension for 2 h at room temperature. The solvent was removed in vacuo using a rotary evaporator, until the weight of the resulting solid was the same as the total weight of **1** and the support before the impregnation procedure. The resulting supported **1** was air-stable and stored in air.

Ammonia synthesis

Ammonia synthesis at an absolute pressure of 1.0 MPa was carried out by use of a vertical continuous-flow fixed-bed reactor with a reaction tube (i.d. 9.4 mm, o.d. 12.7 mm, length 290 mm) made of Inconel which is corrosion-resistant to hydrogen chloride.[2] Typically, a weighed sample of supported cluster **1** (0.2 g) was placed at the center of the tube with the aid of quartz wool and another Inconel tube for fixing the position of the precursor sample, followed by connection of a metal three-way valve and a metal escape pipe to the upper and lower ends of the reaction tube, respectively. The tube was placed in an electric furnace, and the valve was connected to the reactor. The precursor was heated under H_2 flow (300 mL min^{-1}) at atmospheric pressure from room temperature to 600 °C in 1 h and held at the temperature for 3 h. The catalyst was allowed to be cooled to the reaction temperature, and the escape pipe was replaced with a diaphragm back-pressure valve. After stabilization of the temperature, the ammonia synthesis reaction was carried out under N_2/H_2 flow (1:3 molar ratio, 60 mL min^{-1}) at 1.0 MPa. For evaluation of apparent activation energy, the reaction temperature was subsequently changed without changing the other reaction conditions.

Ammonia synthesis at absolute pressures of 2.0–5.0 MPa was carried out by use of an

explosion-proof high-pressure continuous-flow reactor with a piston back-pressure valve (Nakamura Choukou Co., Ltd., custom-made). A weighed supported cluster sample (0.2 g) was first activated under H_2 in the same way as for the activation before ammonia synthesis at 1.0 MPa, followed by cooling to room temperature. Because the resulting activated sample was air-sensitive, the sample was first purged with Ar flow, and a metal two-way valve was connected to the lower end of the Inconel tube during the purge. After the atmosphere inside the tube was replaced with Ar, the valves on both ends were closed, followed by transfer of the tube into the Ar-filled glovebox. The sample was then transferred into the center of an explosion-proof Inconel reaction tube (i.d. 9.4 mm, o.d. 12.7 mm, length 230 mm) with the aid of new quartz wool and another Inconel tube. After connection of an explosion-proof metal three-way valve and a stopper to the upper and lower ends of the reaction tube, respectively, the tube was taken out of the glovebox, placed vertically in an explosion-proof electric furnace (MHI Solution Technologies Co., Ltd., custom-made), and connected to the reactor. The catalyst was heated under N_2/H_2 flow (1:3 molar ratio, 60 mL/min) at atmospheric pressure from room temperature to the reaction temperature in 1 h. After stabilization of the temperature, the ammonia synthesis reaction was carried out under the N_2/H_2 flow at the reaction pressure.

The rate of ammonia formation by use of both reactors was determined by bubbling the vent gas from the back-pressure valve into a 0.0025 M oxalic acid solution, followed by its analysis with an ion chromatography (HIC-20A sp, Shimadzu) with a cation-exchange Shim-pack IC-C4 column (Shimadzu).

Kinetic analysis

The experimental data for determination of the reaction orders were obtained, using the same reaction apparatus as for the ammonia synthesis at 1.0 MPa. To avoid limitations by diffusion and adsorption/desorption, a reduced amount of catalyst (0.025 g) was used.[3] After heating the supported cluster samples under a flow of atmospheric H_2 from room temperature to 600 °C in 1 h and held at 600 °C for 1 h, the reaction was performed under a mixture of N_2, H_2, and Ar with various ratios at 400 °C under 1.0 MPa. The constituent gases of the reactant (N_2, H_2, Ar mL min^{-1}) were as follows: (6, 24, 30), (10, 24, 26), (15, 24, 21), and (22, 24, 14) for N_2 order (n), (5, 24, 31), (5, 30, 25), (5, 42, 13), and (5, 55, 0) for H_2 order (h), and (5, 15, 0), (10, 30, 0), (15, 45, 0), and (20, 60, 0) for NH_3 order (a). The reaction orders were determined according to the published procedure,[4] in which equations (S1) to (S5) were used.

$$r = kP_{N_2}{}^{n} \cdot P_{H_2}{}^{h} \cdot P_{NH_3}{}^{a} \quad \text{(S1)}$$

$$r = (1/w)dy_0/d(1/q) \quad \text{(S2)}$$

$$\log y_0 = \log(C/q)^{1/m} \quad \text{(S3)}$$

$$r = (1/w)(C/m)y_0{}^{(1-m)} \quad \text{(S4)}$$

$$C = k_2 \cdot P_{N_2}{}^{n} \cdot P_{H_2}{}^{h} \quad \text{(S5)}$$

Here, r, w, y_0, q, C, and (1–m) represent ammonia synthesis rate, catalyst mass, ammonia mole fraction at the reactor outlet, flow rate, constant, and the reaction order with respect to NH_3 (a), respectively. Recently, revised equations considering the effect of variation of the P_{NH3} with varying the P_{N2} for determination of the N_2 reaction order have been suggested, and the reaction orders of

around 0.5 for some catalysts have been suggested to increase to nearly 1.0 by use of the revised equations.[5] The present supported Mo metal cluster catalysts showed very slight increase (less than 0.05%) of the N_2 reaction orders, using the revised equations, and therefore the effect could be ignored.

In order to determine the RDS of ammonia synthesis over the supported Mo clusters, the experimental reaction rates were fitted to the calculated rates. When the synthesis reaction is assumed to obey the Langmuir–Hinshelwood (dissociative) mechanism, the following eight elementary steps can be established,[6]

$H_2(gas) + * \rightarrow H_2(ad)$ (S6)

$N_2(gas) + * \rightarrow N_2(ad)$ (S7)

$H_2(ad) + * \rightarrow 2H(ad)$ (S8)

$N_2(ad) + * \rightarrow 2N(ad)$ (S9)

$N(ad) + H(ad) \rightarrow NH(ad) + *$ (S10)

$NH(ad) + H(ad) \rightarrow NH_2(ad) + *$ (S11)

$NH_2(ad) + H(ad) \rightarrow NH_3(ad) + *$ (S12)

$NH_3(ad) \rightarrow NH_3(gas) + *$ (S13)

where * denotes the vacant site, and (gas) and (ad) mean gas-phase and adsorption species, respectively. Among these reaction step, steps (S9)–(S12) control the overall reaction rate owing to the large activation energy. Because the partial pressure of NH_3 (P_{NH3}) was much smaller than that of N_2 (P_{N2}) and H_2 (P_{H2}) at the outlet under the reaction conditions employed, the P_{NH3} was omitted. Finally, the following four rate equations were obtained.

$$r = \frac{\vec{k}_4 K_2 P_{N_2}}{\left(1+K_1 P_{H_2}+K_2 P_{N_2}+\sqrt{K_1 K_3 p_{H_2}}\right)^2} \quad \text{(S14)}$$

$$r = \frac{\vec{k}_5 \sqrt{K_1 K_2 K_3 K_4} \sqrt{P_{H_2} P_{N_2}}}{\left(1+K_1 P_{H_2}+K_2 P_{N_2}+\sqrt{K_1 K_3 P_{H_2}}+\sqrt{K_2 K_4 P_{N_2}}\right)^2} \quad \text{(S15)}$$

$$r = \frac{\vec{k}_6 K_1 K_3 K_5 \sqrt{K_2 K_4} P_{H_2} \sqrt{P_{N_2}}}{\left(1+K_1 p_{H_2}+K_2 p_{N_2}+\sqrt{K_1 K_3 P_{H_2}}+\sqrt{K_2 K_4 P_{N_2}}+K_5 \sqrt{K_1 K_2 K_3 K_4 P_{H_2} P_{N_2}}\right)^2} \quad \text{(S16)}$$

$$r = \frac{\vec{k}_7 K_1 K_3 K_5 K_6 \sqrt{K_1 K_2 K_3 K_4} P_{H_2} \sqrt{P_{H_2} P_{N_2}}}{\left(1+K_1 P_{H_2}+K_2 P_{N_2}+\sqrt{K_1 K_3 P_{H_2}}+\sqrt{K_2 K_4 P_{N_2}}+K_5 \sqrt{K_1 K_2 K_3 K_4 P_{H_2} P_{N_2}}+K_1 K_3 K_5 K_6 \sqrt{K_2 K_4 P_{N_2}} P_{H_2}\right)^2} \quad \text{(S17)}$$

where $\vec{k}_i$ is the rate constant for the forward reactions and K_i is the equilibrium constant in step i. Equations (S14)–(S17) are based on the assumption that the steps (S9)–(S12) are the RDS, respectively. For determination of the RDS for ammonia synthesis over the cluster on HY, the derived equations were separately fitted into sets of experimental rates using a least squares method and evaluated to determine which equations best described the experimental rates.

Characterization

Supported cluster samples after impregnation, H_2-activation for 3 h at 600 °C under atmospheric pressure, and ammonia synthesis for 4 h at 400 °C under 1.0 MPa were prepared separately for characterization. The samples after the H_2-activation and the ammonia synthesis were air-sensitive. Thus, the sample after each of these treatments was purged with a flow of Ar under

atmospheric pressure, and the lower end of the reaction tube was connected to a stainless two-way valve during the purge. After the atmosphere inside the tube was replaced with Ar, the stainless valves on both sides of the tube were closed, followed by transfer of the tube to the Ar-filled glovebox. The sample inside the tube was collected into a glass bottle for further analysis.

X-ray absorption fine structure (XAFS) of the supported cluster samples were measured, using a T-shaped Pyrex-glass cell composed of a vertical part (30 mm length and 12.7 mm diameter) and a horizontal part (10 mm length and 8 mm diameter) with Pyrex-glass windows (0.3 mm thickness) at both ends of the horizontal part. The samples after impregnation (ca. 0.6 g) were introduced from the open end of the vertical part and sealed with a Swagelok fitting in air. The samples after the H_2-activation and the ammonia synthesis were prepared from 0.2 g of the precursor several times, collected, and packed in the cell in the same way as for the samples after impregnation. As standard samples, boron nitride-diluted unsupported cluster **1** was measured in the same way as for the samples after impregnation, whereas Na_2MoO_4 was measured in the form of a film. All the measurements were carried out using a synchrotron radiation ring at the BL5S1 or BL11S2 of Aichi Synchrotron Radiation Center with an Si (111) double-crystal monochromator in transmission mode. The energy of the X-ray was calibrated using the molybdenum foil. The XANES spectra were normalized to unity by their edge jumps. The EXAFS spectra were analyzed by the RIGAKU REX2000.[7] After background subtraction, a k^3-weighted EXAFS spectrum in the k range of 3.0–14.5 $Å^{-1}$ was Fourier-transformed into an R-space. The main peak region in the resulting FT-EXAFS spectrum was filtered and inversely Fourier-transformed into k space. The curve fitting analyses were carried out in the k range of 3.0–11.5, 3.0–14.0, and 3.0–14.5 $Å^{-1}$ for **1**/MCM41 after the H_2-activation or the ammonia synthesis, **1**/HY after the H_2-activation or the ammonia synthesis, and the other samples, respectively. The standard cluster sample **1** and the cluster after impregnation showed one major peak in the main peak region, and the peak was fitted with a Mo–Mo shell and a Mo–Cl shell. Clusters on HZSM5 after H_2-activation and after ammonia synthesis exhibited FT-EXAFS spectra similar to that of metallic molybdenum with the base-centered cubic (bcc) structure. The region has two peaks which are attributed to the nearest and next nearest Mo–Mo with a coordination number ratio of 8 and 6, respectively. Thus, the two peaks were fitted with two Mo–Mo shells by fixing the coordination number ratio of 4:3. Clusters on HY after H_2-activation and after NH_3-synthesis included a bond between Mo and oxygen of the support. Thus, the two peaks in the main peak region in the FT-EXAFS spectra were fitted with a Mo–Mo shell and a Mo–O shell. The analysis for clusters on MCM41 after H_2-activation and after ammonia synthesis was performed in the same way as for the clusters on HY. The Fourier-filtered data were then analyzed by means of the least-square curve-fitting method using the following equations (S18) and (S19),[8]

$$\chi(k) = \sum_i \frac{S_i N_i F_i(k_i) \mathrm{e}^{-2\sigma_i{}^2 k_i{}^2}}{k_i r_i{}^2} \sin\left(2k_i r_i + \varphi_i(k_i)\right) \qquad \text{(S18)}$$

$$k_i = \sqrt{k^2 - 2m_e \Delta E_i/\hbar^2} \qquad \text{(S19)}$$

where S_i, N_i, σ_i, and r_i, are an inelastic reduction factor, a coordination number (CN), a Debye–Waller factor, and a bond distance for i-th shell, respectively. $F_i(k)$ and $\varphi_i(k)$ are a backscattering amplitude and a phase shift function for i-th shell, respectively. The amplitudes and phase shifts were calculated

by the FEFF8 code.[9] ΔE_i is a difference between experimentally determined photoelectron kinetic energy zero and that used for theoretical calculation for phase shift and amplitude functions of the *i*-th shell. The fitted parameters were N_i, σ_i, r_i, and ΔE_i. The error of these four parameters was estimated using the Hamilton ratio test with a significance level of 0.317.[10] A goodness of the fitting was evaluated using *R* factor defined as the equation (S20).

$$R = \frac{\Sigma\left(k^3\chi_{\mathrm{obs}}(k)-k^3\chi_{\mathrm{calc}}(k)\right)^2}{\Sigma\left(k^3\chi_{\mathrm{obs}}(k)\right)^2} \qquad \text{(S20)}$$

The N_i values of the supported cluster samples were corrected by S_i factors which were obtained from standard samples such as unsupported cluster **1** for Mo–Mo (0.64(0.04)) and Mo–Cl shells (0.79(0.03)) and Na_2MoO_4 for Mo–O shell (1.1(0.2)).

STEM measurements were performed using a JEM-2100F/SP microscope operating at 200 kV. High-resolution STEM (HRSTEM) imaging, using a high-angle annular dark-field detector (HAADF), was performed using a FEI Titan Cubed G2 60-300 operated at 300 kV and equipped with a Cs probe corrector (DCOR from CEOS GmbH), a monochromator, and an ultra-bright X-FEG electron source. The convergence angle was 17.9 mrad. The typical probe current was set to 50 pA and the total dose on the sample varied between ~0.2–3 C cm^{-2} under the HRSTEM imaging conditions, which corresponds to low-dose conditions.[11]

H_2-TPR measurement was performed using a BELCAT-A catalyst analyzer (MicrotracBEL Co.) equipped with a thermal conductivity detector (TCD). Prior to the measurement, the catalyst sample (0.03 g) was preheated at 300 °C for 10 min and cooled to 40 °C in a helium stream (30 mL/min). Subsequently, the sample was heated up to 600 °C in 5% H_2/Ar feed (30 mL/min) at 10 °C/min.

Ammonia pulse measurements were performed using a BELCAT II catalyst analyzer (MicrotracBEL Co.) equipped with a TCD. Each inlet and outlet of the sample holder had a three-way valve which was connected to each other by a bypass line. In the Ar-filled glovebox, a weighed sample (0.04 g) of the supported clusters or only the supports after the H_2-activation was loaded in a quartz tube reactor, and the reactor was attached to the holder where the three-way valves were closed. Then the reactor was taken out of the glovebox and installed on the analyzer. After turning the valves to the bypass line and purging the line with a helium flow for ca. 20 min, the valves were turned to the reactor. The sample was heated up to 600 °C in 1 h and kept for 1 h in a hydrogen stream (100 mL/min), followed by treatment with a helium flow (80 mL/min) for 30 min for removal of gaseous hydrogen and cooling down to 100 °C in the helium stream. Then ammonia diluted with helium (ca. 10%) was pulsed to the sample at 100 °C using pure helium as the carrier gas, until the amount of ammonia at the outlet reached a constant value. The ammonia desorbed was monitored by the TCD detector. Pore volume and Brunauer–Emmett–Teller (BET) surface areas were determined using a BELSORP-maxII (MicrotracBEL Co.). A weighed sample (80 mg) of the supported clusters and only the supports after the H_2-treatment or the ammonia synthesis was loaded in a glass sample cell in Ar atmosphere. Then the sample was evacuated at 300 °C for 12 h, followed by measurement of nitrogen adsorption−desorption isotherms at –196 °C. The BET and t-plot methods were used for estimation of the surface area and the pore volume, respectively.

Computational Methods

DFT calculations

All DFT calculations were performed using the Gaussian 16 program package.[12] The B3LYP functionals with the def2-TZVP basis set were employed for H and N atoms, while the same type of basis set was used for Mo atoms in conjunction with the effective core potential. In geometry optimization, no symmetry constraint was imposed. To model the catalytic reaction on Y-zeolite, we first investigated the stable structures of the Mo_6 cluster on Y-zeolite. To reduce the computational cost, we cut local ring structures of Y-zeolite taken from the database, and three types of local structures, denoted as (4+4)R, 6R, (4+6)R, were compared (see Fig. S18). (4+4)R represents the two adjacent four-membered oxygen rings, and 6R denotes the six-membered oxygen ring. (4+6)R is the local structure of the adjacent four-membered and six-membered oxygen rings. The Si−O bonds which are outside the ring structures are terminated and capped by hydrogen atoms, and all Si atoms in the rings are fixed to the crystal structure during the geometry optimization. We placed the Mo_6 cluster on the above three local structures, and the formation energy of the Mo_6 cluster is compared. The most stable structures of Mo_6 at each local structure are shown in Fig. S18. In (4+4)R model, the structure denoted as (4+4)R-I exhibits the strongest formation energy, and in this structure, three Mo atoms coordinate to the zeolite O atoms. We employ this structure in the investigation of the reaction mechanism throughout this paper. The interatomic distances of the Mo_6 cluster at the optimized structures are given in Table S6.

The adsorption energies of N_2, H_2, and intermediates in the reaction profiles were calculated according to

$$\Delta E_{\mathrm{ad}} = E_{\mathrm{mol+Mo_6@HY}} - E_{\mathrm{mol}} - E_{\mathrm{Mo_6@HY}}$$

where $E_{\mathrm{mol+Mo_6@HY}}$ is the total electronic energy of the system while $E_{\mathrm{Mo_6@HY}}$ and E_{mol} are the energies of optimized Mo6@HY model mentioned above and isolated molecular species, respectively. In this definition, the more negative value of adsorption energy indicates a stronger binding to the catalyst. The zero-point energies are included in the above definition, where only the vibrational frequencies of the adspecies were taken into account, while all Mo atoms and atoms in the zeolite framework are fixed.

Microkinetic Analysis

A microkinetic model[13] was constructed to determine the dominant reaction pathway among all possible ones obtained by DFT calculations. In this model, a structure of multiple adsorbents on the Mo_6 cluster was defined as one state, and the adsorption states such as μ_2- and μ_3-bridging N were distinguished. Using this model, it is possible to distinguish the pathways and discuss the reaction flow. Fig. S19 shows the potential energy diagram with the reaction flow determined by the microkinetic model. The dissociative pathway with the μ_3-briding N and NH_x pathway through **B1** to **B8** accounts for almost 99 % of the total reaction flow, and there is only less than 0.001 % of the reaction flow in the associative pathways C and D.

Tables and Figs.

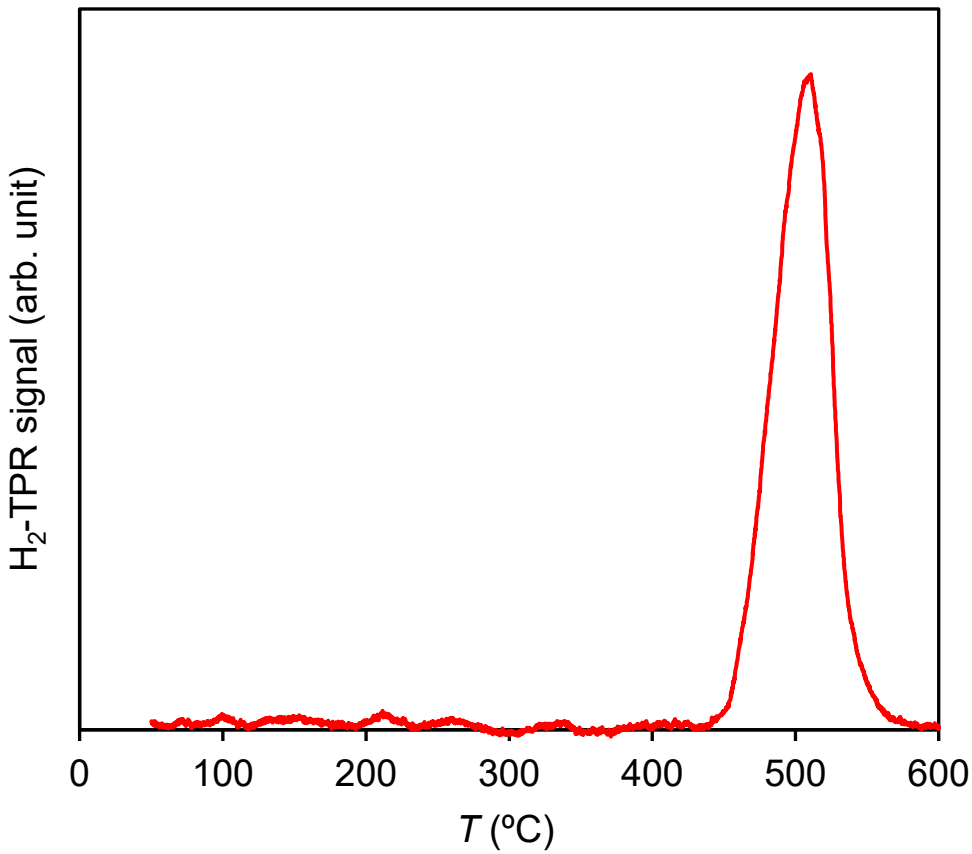

Fig. S1. H_2-TPR profile of $(H_3O)_2[(Mo_6Cl_8)Cl_6]\cdot 6H_2O$ (**1**)/HY.

Table S1. Elemental analysis results of supported Mo clusters.

Sample	After impregnation		After H_2-activation[a]		After NH_3-synthesis[b]	
	Mo (wt%)	Cl (wt%)	Mo (wt%)	Cl (wt%)	Mo (wt%)	Cl (wt%)
$(H_3O)_2[(Mo_6Cl_8)Cl_6]\cdot 6H_2O$ (**1**)/HY	2.4	1.9	2.6	0.0	2.6	0.0
$(H_3O)_2[(Mo_6Cl_8)Cl_6]\cdot 6H_2O$ (**1**)/HZSM5	2.4	1.9	2.5	0.0	2.5	0.0
$(H_3O)_2[(Mo_6Cl_8)Cl_6]\cdot 6H_2O$ (**1**)/MCM41	2.3	1.9	2.6	0.0	2.5	0.0

[a] Samples after impregnation were heated at 600 °C and atmospheric pressure for 3 h under H_2 flow (300 mL). [b] Samples after the H_2-activation were subsequently subjected to N_2/H_2 flow (1:3 molar ratio, 60 mL min^{-1}) at 400 °C and 1.0 MPa (absolute pressure) for 4 h.

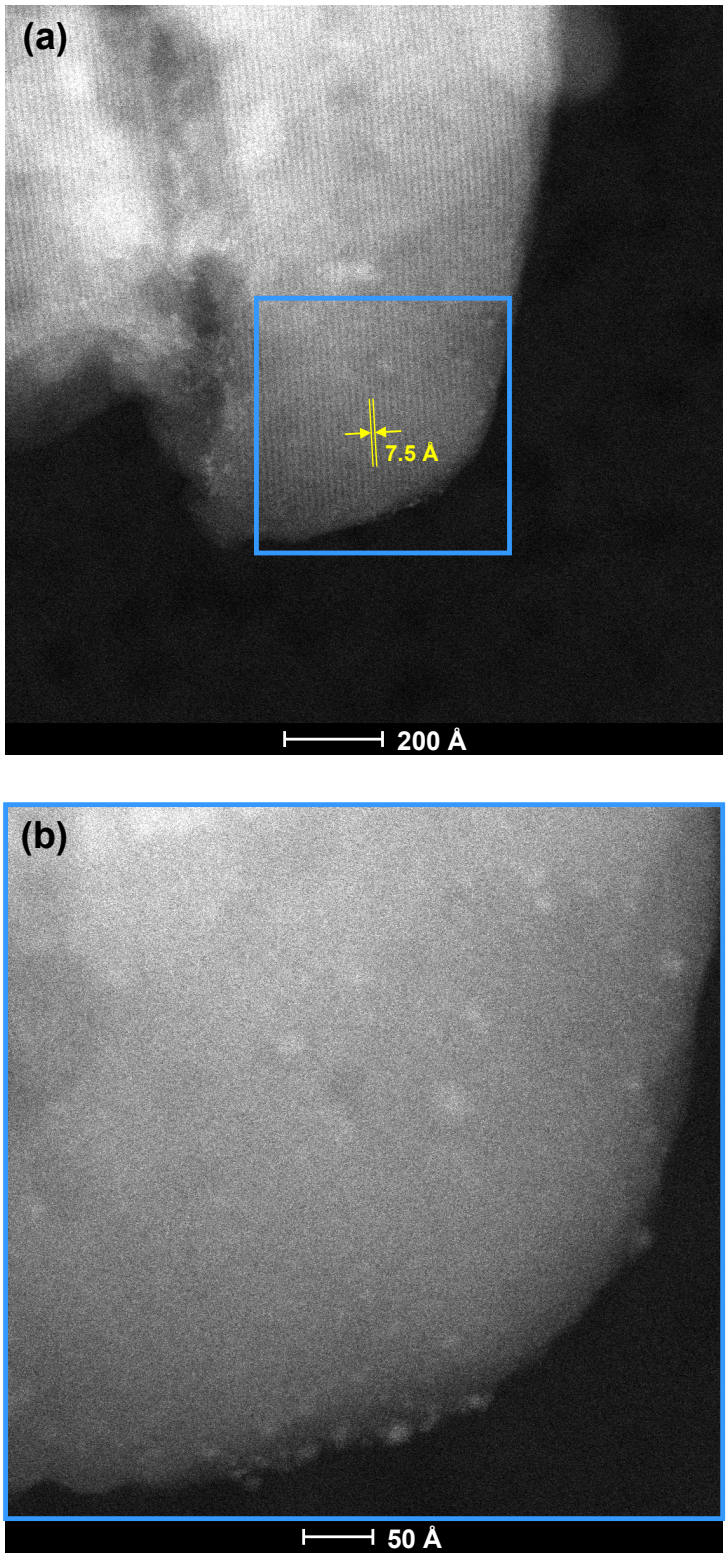

Fig. S2. STEM images of $(H_3O)_2[(Mo_6Cl_8)Cl_6]\cdot 6H_2O$ (**1**)/HY after impregnation. (b) is an enlargement of the blue frame of (a). The pore stripes for (b) disappeared during the measurement owing to irradiation of the high-energy electron beam. Only the particles surrounded by the blue frame were analyzed because of no overlap of the HY layers.

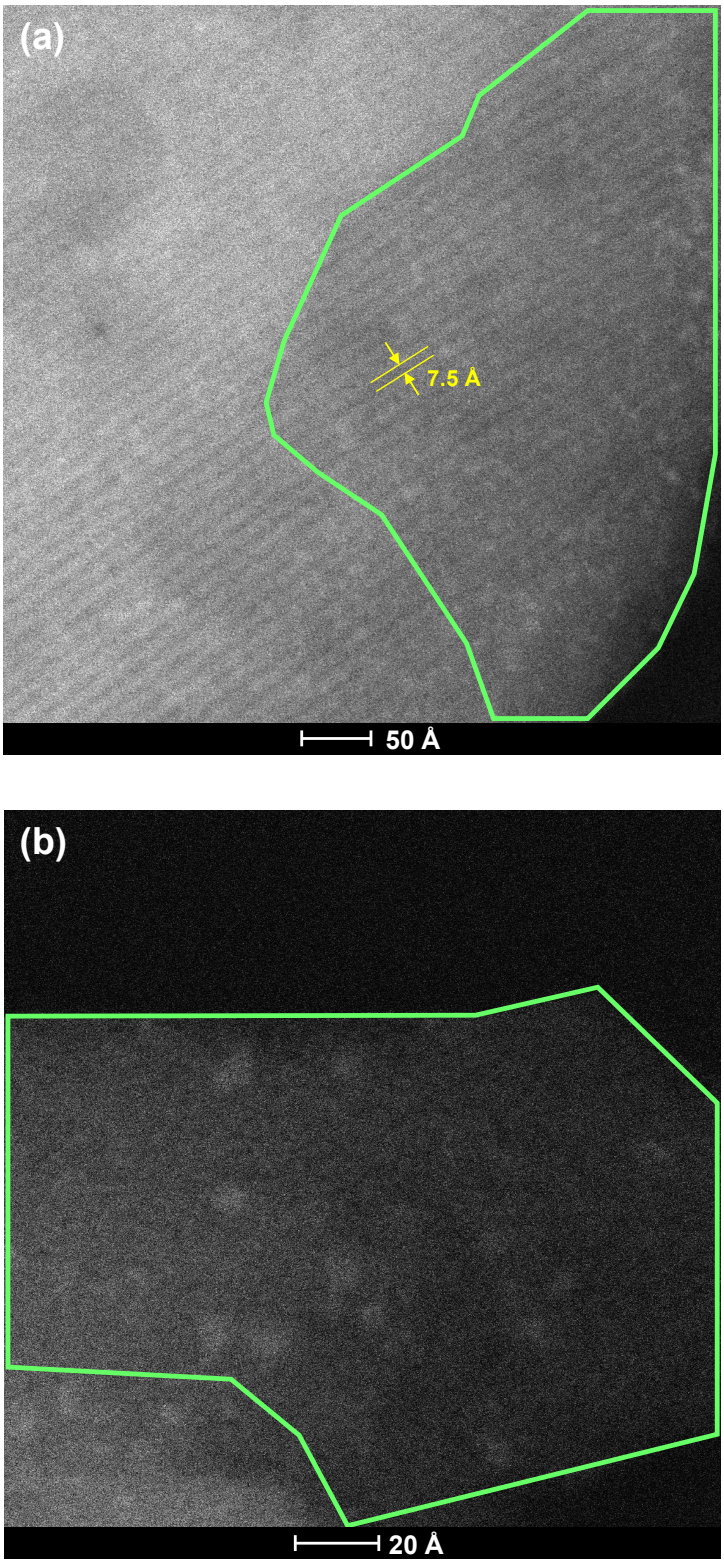

Fig. S3. STEM images of $(H_3O)_2[(Mo_6Cl_8)Cl_6]\cdot 6H_2O$ (**1**)/HY after H_2-activation. Only the particles surrounded by the green frame in (a) and (b) were analyzed because of no overlap of the HY layers. The pore stripes for (b) disappeared during the measurement owing to irradiation of the high-energy electron beam.

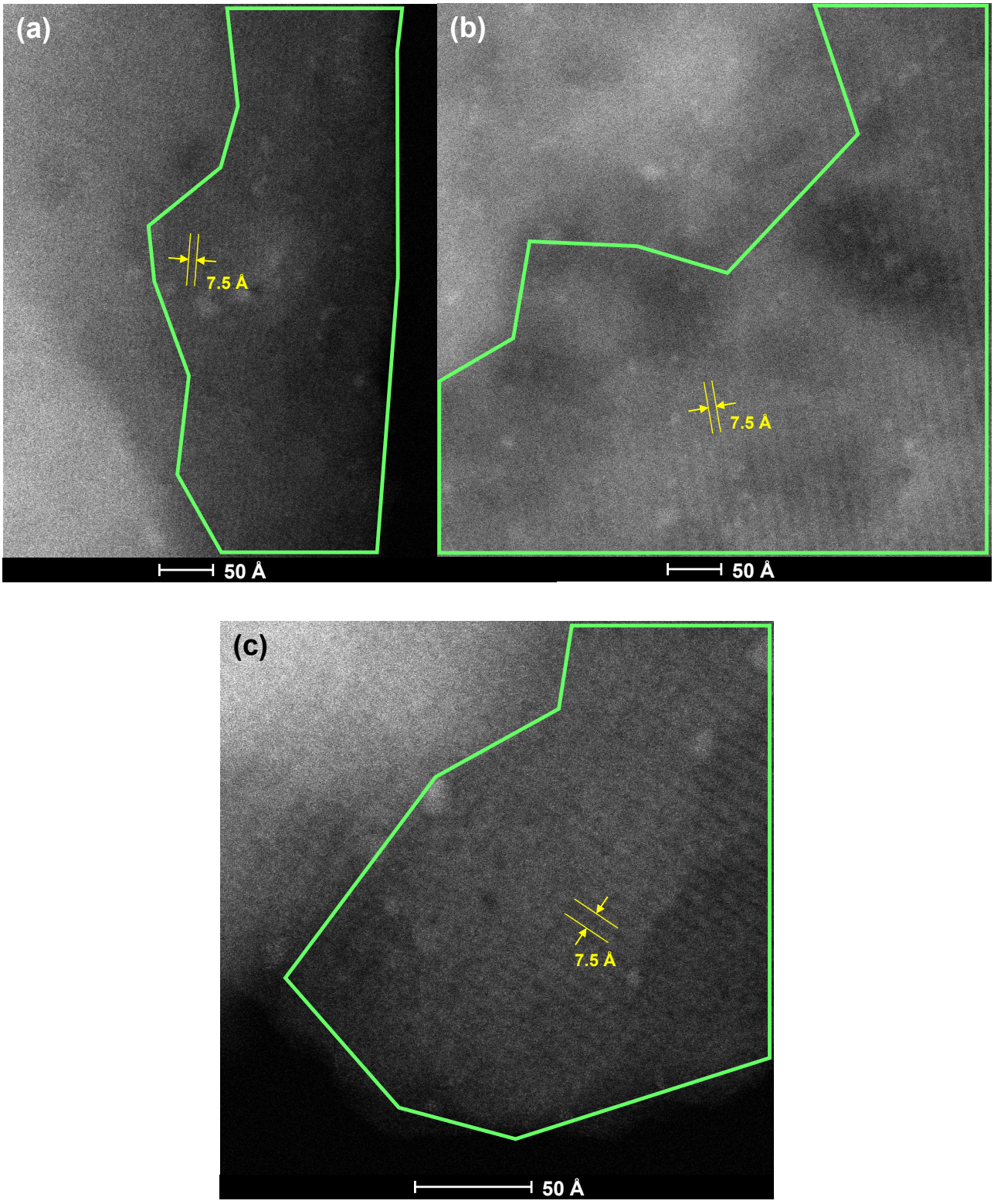

Fig. S4. STEM images of $(H_3O)_2[(Mo_6Cl_8)Cl_6]\cdot 6H_2O$ (**1**)/HY after ammonia synthesis. Only the particles surrounded by the green frame in (a), (b), and (c) were analyzed because of no overlap of the HY layers.

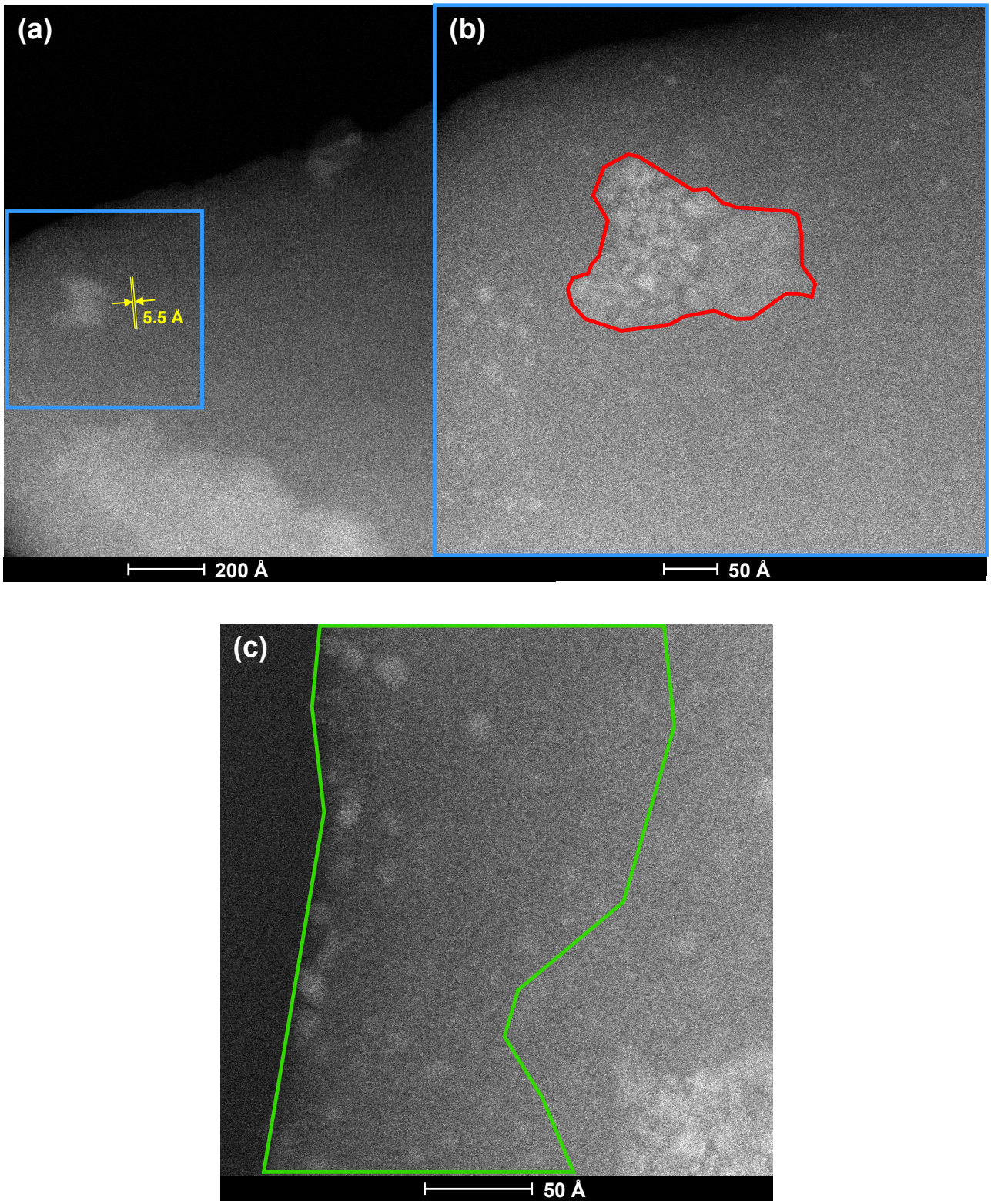

Fig. S5. STEM images of $(H_3O)_2[(Mo_6Cl_8)Cl_6]\cdot 6H_2O$ (**1**)/HZSM5 after impregnation. (b) is an enlargement of the blue frame of (a). The pore stripes for (b) and (c) disappeared during the measurement owing to irradiation of the high-energy electron beam. In (a) and (b), only the particles surrounded by the blue frame except surrounded by the red frame were analyzed because of no overlap of the HZSM5 layers. In (c), only the particles surrounded by the green frame were analyzed because of no overlap of the HZSM5 layers.

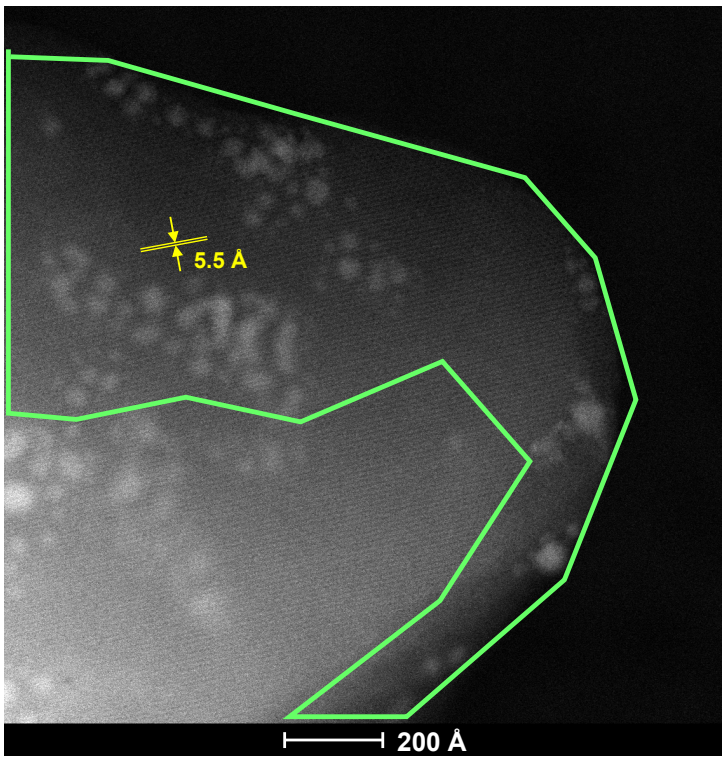

Fig. S6. STEM images of $(H_3O)_2[(Mo_6Cl_8)Cl_6]\cdot 6H_2O$ (**1**)/HZSM5 after H_2-activation. Only the particles surrounded by the green frame were analyzed because of no overlap of the HZSM5 layers.

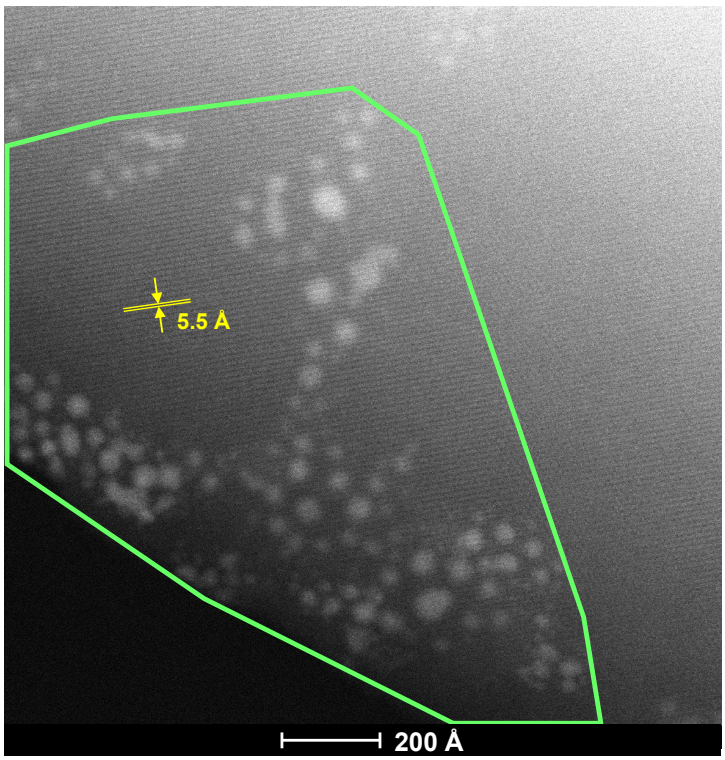

Fig. S7. STEM images of $(H_3O)_2[(Mo_6Cl_8)Cl_6]\cdot 6H_2O$ (**1**)/HZSM5 after ammonia synthesis. Only the particles surrounded by the green frame were analyzed because of no overlap of the HZSM5 layers.

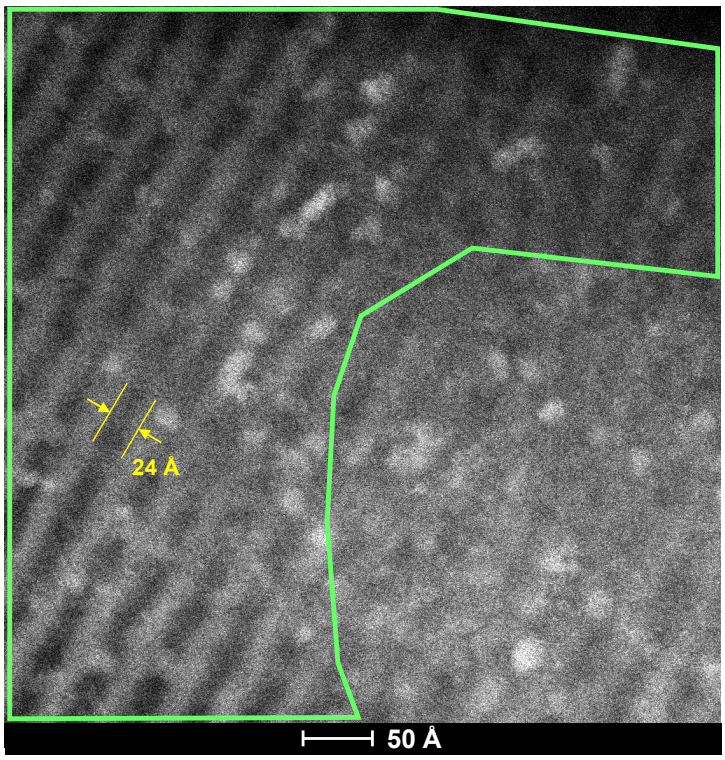

Fig. S8. STEM images of $(H_3O)_2[(Mo_6Cl_8)Cl_6]\cdot 6H_2O$ (**1**)/MCM41 after impregnation. Only the particles surrounded by the green frame were analyzed because of no overlap of the MCM41 layers.

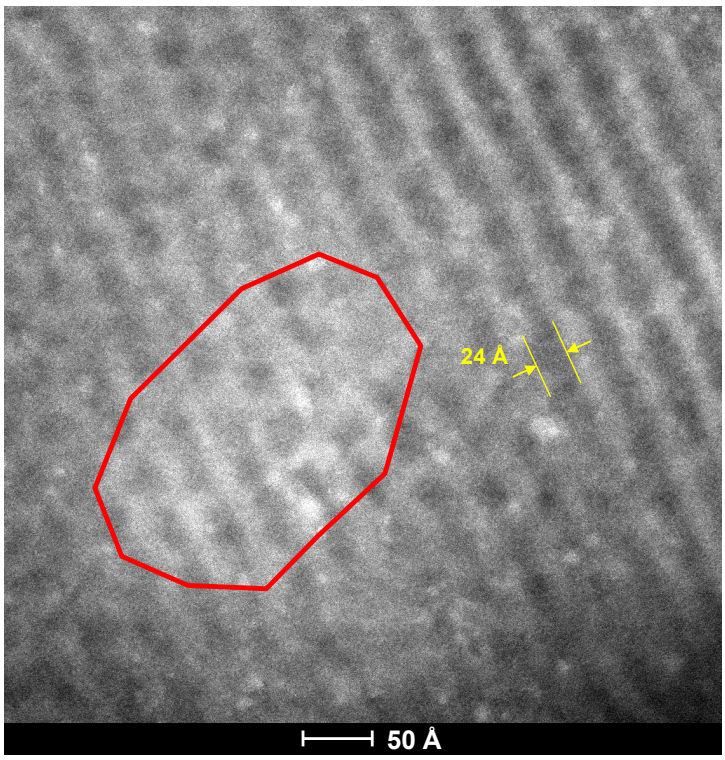

Fig. S9. STEM images of $(H_3O)_2[(Mo_6Cl_8)Cl_6]\cdot 6H_2O$ (**1**)/MCM41 after H_2-activation. The particles except surrounded by the red frame were analyzed because of no overlap of the MCM41 layers.

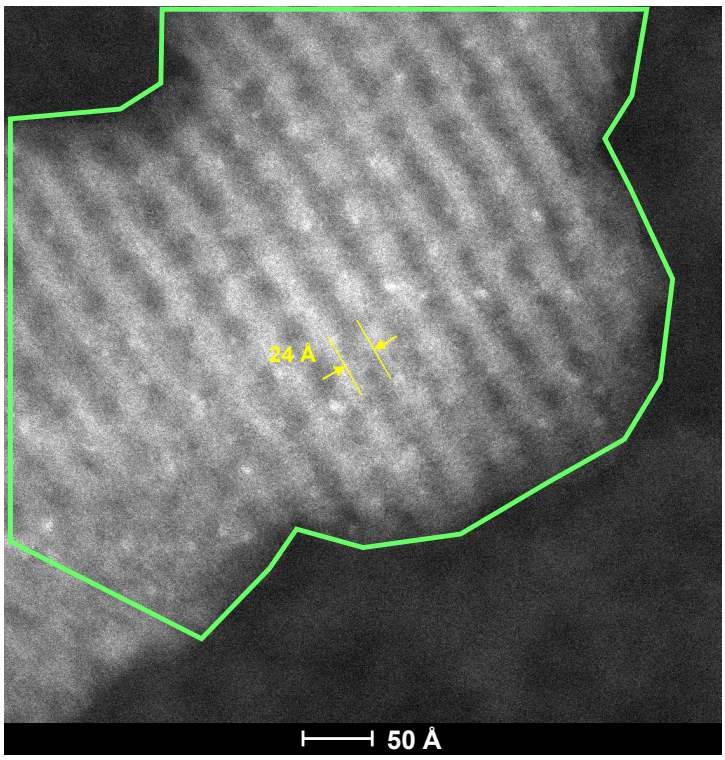

Fig. S10. STEM images of $(H_3O)_2[(Mo_6Cl_8)Cl_6]\cdot 6H_2O$ (**1**)/MCM41 after ammonia synthesis. Only the particles surrounded by the green frame were analyzed because of no overlap of the MCM41 layers.

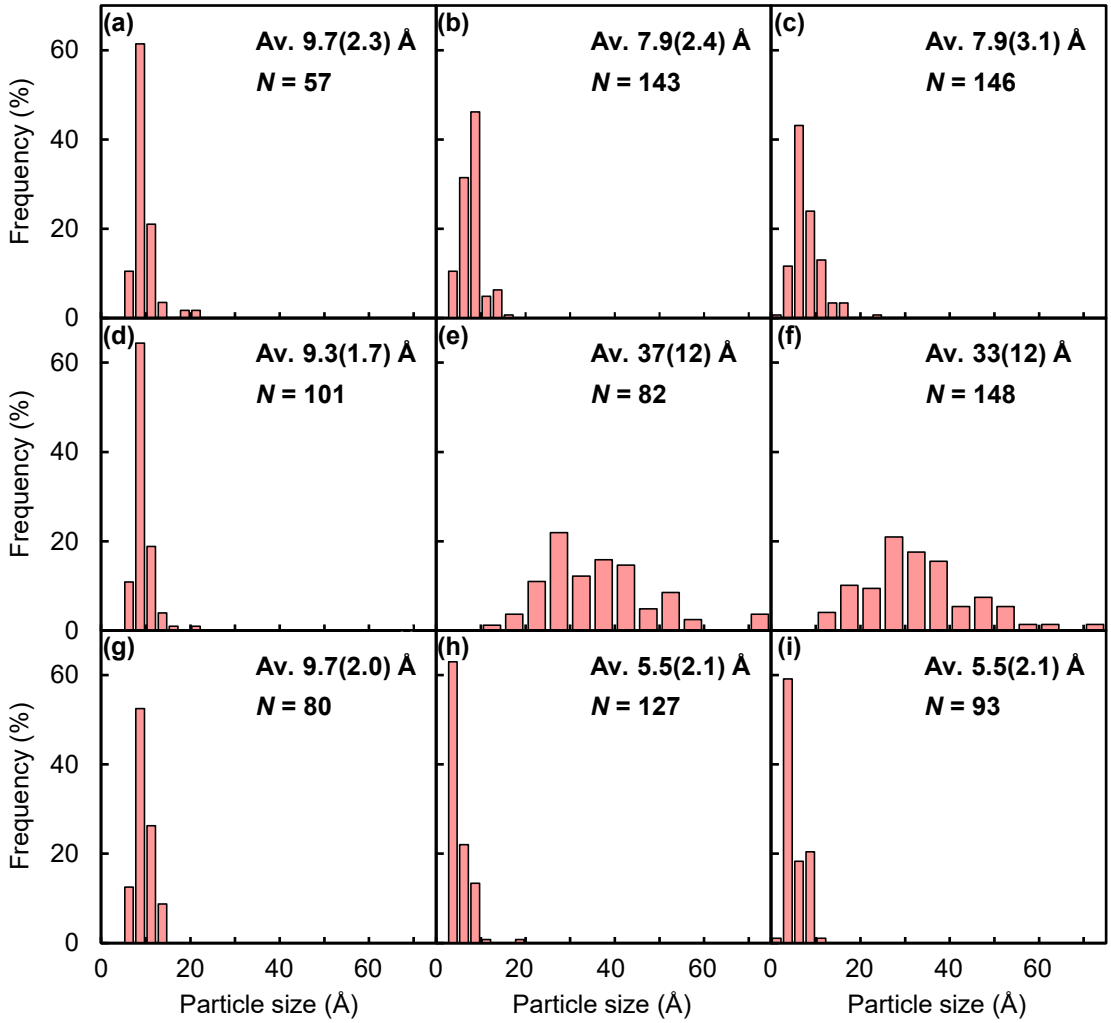

Fig. S11. STEM particle size distributions of $(H_3O)_2[(Mo_6Cl_8)Cl_6]\cdot 6H_2O$ (**1**)/HY (a) after impregnation, (b) after H_2-activation, and (c) after NH_3-synthesis, **1**/HZSM5 (d) after impregnation, (e) after H_2-activation, and (f) after NH_3-synthesis, and **1**/MCM41 (g) after impregnation, (h) after H_2-activation, and (i) after NH_3-synthesis. The values in the parentheses are standard deviations, and *N* represents the number of particles analyzed.

Table S2. Surface properties of H_2-activated HY with and without loading of $(H_3O)_2[(Mo_6Cl_8)Cl_6]\cdot 6H_2O$ (**1**).

Catalyst (Precursor)	Surface area (m^2 g-cat^{-1})[a]	Pore volume (cm^3 g-cat^{-1})[a]
$(H_3O)_2[(Mo_6Cl_8)Cl_6]\cdot 6H_2O$ (**1**)/HY	810	0.286
HY	850	0.298

[a] After H_2-activation.

The pore volume of Mo cluster-loaded HY (0.286 cm^3 g-cat^{-1}) was smaller than that of HY without the cluster (0.298 cm^3 g-cat^{-1}), after the same H_2-treatment. The difference (0.012 cm^3 g-cat^{-1} = 0.48 cm^3 g-Mo^{-1}) was comparable to the reported values (0.6 cm^3 g-$metal^{-1}$).[14]

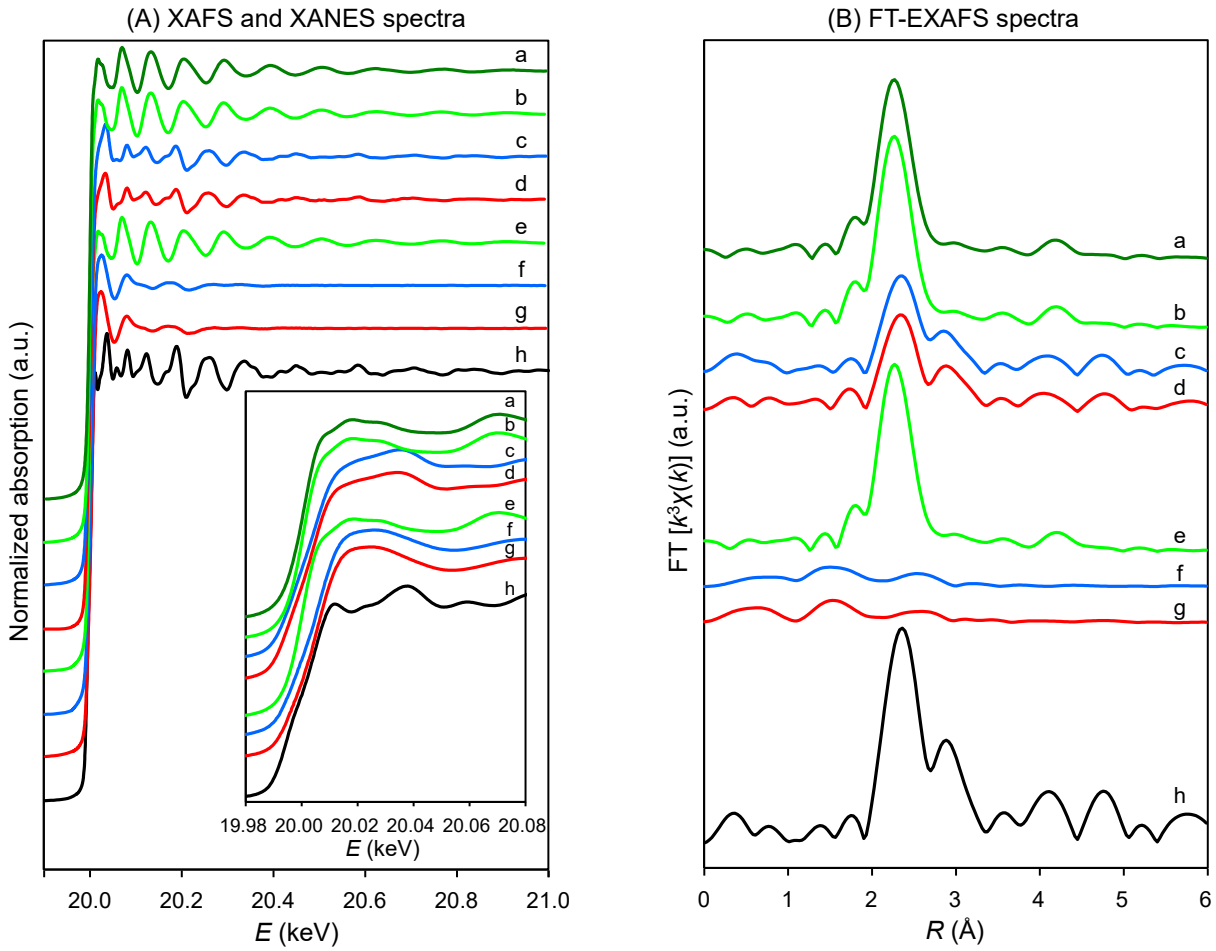

Fig. S12. (A) XAFS of $(H_3O)_2[(Mo_6Cl_8)Cl_6]\cdot 6H_2O$ (**1**). The inset shows the XANES region. (B) FT-EXAFS spectra of **1**. (a) As prepared, (b) **1**/HZSM5 after impregnation, (c) **1**/HZSM5 after H_2-activation, (d) **1**/HZSM5 after ammonia synthesis, (e) **1**/MCM41 after impregnation, (f) **1**/MCM41 after H_2-activation, and (g), **1**/MCM41 after ammonia synthesis. Spectra of Mo foil from Spring-8 BENTEN database (h) are also shown.

The XAFS and FT-EXAFS spectra of **1**/HZSM5 before impregnation (Figs. S12Aa and S12Ba) were very similar to those of **1**/HZSM5 after impregnation (Figs. S12Ab and S12Bb), indicating no molecular structure change of **1** after the impregnation. After the H_2-activation, the spectra (Figs. S12Ac and S12Bc) became similar to those of the bcc Mo metal (Figs. S12Ah and S12Bh), demonstrating the conversion of **1** to Mo metal on HZSM5. **1**/MCM41 also exhibited almost no difference in the XAFS and FT-EXAFS spectra between before (Figs. S12Aa and S12Ba) and after impregnation (Figs. S12Ae and S12Be). After H_2-activation, the FT-EXAFS spectrum afforded two small peaks at 1.5 and 2.5 Å (Fig. S12Bf), and the curve fitting analysis (Table S3, see next page) attributes the former and latter peaks to Mo–O (oxygen on the HY) with a CN of 2.0 and Mo–Mo with a CN of 3.0, respectively. This Mo–Mo CN is lower than that of **1** (4.0) and even that of the H_2-activated **1**/HY (3.6) (Table 1). These results indicate that the Mo_6 cluster afforded a smaller Mo cluster on MCM41 by the H_2-activation.

Table S3. Curve fitting results of Mo K-edge EXAFS data

Sample	Conditions	Shell	CN[a]	R/Å[a]	$\sigma/10^{-2}$ Å[a]	R_f/%[b]
$(H_3O)_2[(Mo_6Cl_8)Cl_6]\cdot 6H_2O$ (**1**)	As prepared[c]	Mo–Mo	4.0 (Fixed)	2.65(0.01)	2.2(0.7)	0.14
		Mo–Cl	5.0 (Fixed)	2.54(0.01)	1.3(1.3)	
$(H_3O)_2[(Mo_6Cl_8)Cl_6]\cdot 6H_2O$ (**1**)/HZSM5	After impregnation	Mo–Mo	4.2(0.3)	2.65(0.01)	2.3(0.6)	0.10
		Mo–Cl	5.3(0.2)	2.54(0.01)	1.3(1.3)	
	After H_2-activation	Mo–Mo	5.5(0.6)	2.73(0.01)	5.2(0.4)	1.8
		Mo–Mo	4.1(0.5)	3.14(0.01)	4.9(0.5)	
	After NH_3-synthesis	Mo–Mo	5.2(0.7)	2.73(0.01)	5.0(0.5)	2.7
		Mo–Mo	3.9(0.5)	3.15(0.01)	4.6(0.6)	
$(H_3O)_2[(Mo_6Cl_8)Cl_6]\cdot 6H_2O$ (**1**)/MCM41	After impregnation	Mo–Mo	4.1(0.5)	2.65(0.01)	2.1(1.1)	0.11
		Mo–Cl	5.3(0.3)	2.54(0.01)	1.6(1.6)	
	After H_2-activation	Mo–Mo	3.0(1.3)	2.73(0.03)	9.5(1.8)	1.7
		Mo–O	2.0(0.5)	2.04(0.02)	7.3(1.8)	
	After NH_3-synthesis	Mo–Mo	3.0(1.3)	2.75(0.04)	10.0(1.7)	1.4
		Mo–O	1.9(0.4)	2.03(0.02)	6.6(1.6)	

[a] Numbers in parentheses are errors estimated using the Hamilton ratio test with a significance level of 0.317.[10] [b] The good fit of the observed and calculated data was also demonstrated by EXAFS-fitting curves shown in Fig. S13 (a), (e)–(j). [c] Sample diluted with boron nitride was analyzed.

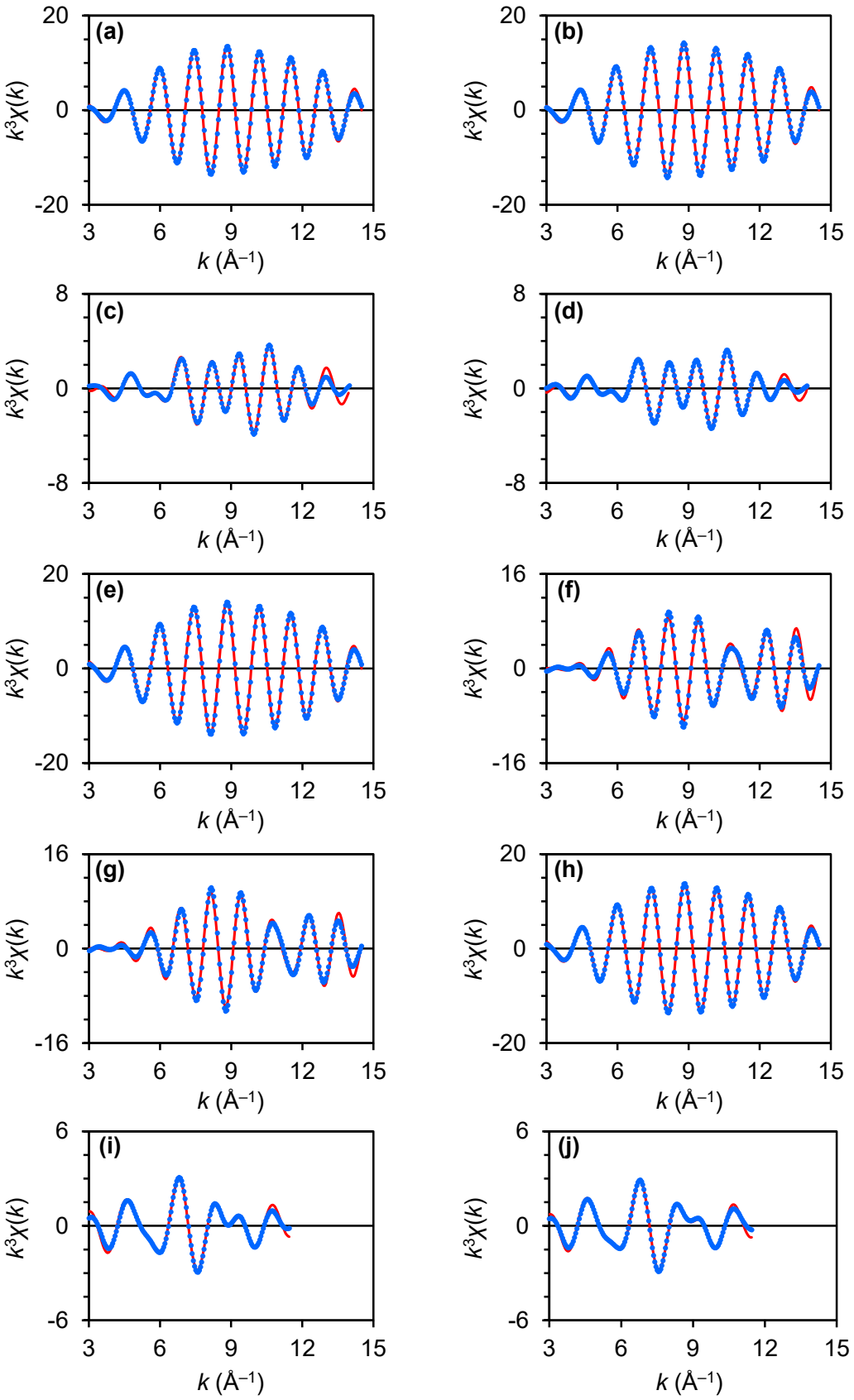

Fig. S13. EXAFS fitting curves of (a) $(H_3O)_2[(Mo_6Cl_8)Cl_6]\cdot 6H_2O$ (**1**) before impregnation, and **1**/HY (b) after impregnation, (c) after H_2-activation, and (d) after NH_3-synthesis, **1**/HZSM5 (e) after impregnation, (f) after H_2-activation, and (g) after NH_3-synthesis, and **1**/MCM41 (h) after impregnation, (i) after H_2-activation, and (j) after NH_3-synthesis. Blue dotted and red solid lines are observed and calculated data, respectively.

Table S4. Catalytic properties of supported Mo metal cluster catalysts.

Catalyst (Precursor)	Surface area (m^2 g-cat^{-1})[a]	Pore volume (m^3 g-cat^{-1})[a]	Adsorbed NH_3[b, c] (cm^3 g-cat^{-1})			NH_3 synthesis Rate[b] (mmol g_{Mo}^{-1} h^{-1})	TOF (s^{-1})[e]
			Mo cluster /support	Support	Mo cluster[d]		
$(H_3O)_2[(Mo_6Cl_8)Cl_6]\cdot 6H_2O$ (**1**) /HY	810	0.296	0.60(0.03)	0.02(0.03)	0.58(0.04)	10.2(0.7)	0.006[f]
$(H_3O)_2[(Mo_6Cl_8)Cl_6]\cdot 6H_2O$ (**1**) /HZSM5	405	0.155	0.80(0.04)	0.41(0.02)	0.39(0.05)	14.7(1.1)	0.006[f]
$(H_3O)_2[(Mo_6Cl_8)Cl_6]\cdot 6H_2O$ (**1**) /MCM41	930	0.712	0.67(0.03)	0.25(0.03)	0.42(0.04)	20.5(0.7)	0.004[f]

[a] After ammonia synthesis. [b] The experiments were performed three times, and the values in the parentheses are standard deviations. [c] N_2, H_2, and CO were not adsorbed on any samples. [d] The NH_3 adsorption amount on Mo cluster was estimated by subtracting the measured NH_3 adsorption amount on Mo cluster-loaded support from that on only support. [e] Calculated from the ammonia synthesis rate divided by the NH_3-adsorbing Mo atoms. [f] The standard deviation was less than 0.001.

Table S5. Summary of data for various ammonia synthesis catalysts at 400 °C

Entry	Catalyst (Precursor)	Metal ratio (wt%)	NH_3 synthesis rate (mmol g_{Mo}^{-1} h^{-1})	NH_3 synthesis rate (mmol g_{cat}^{-1} h^{-1})	Outlet ammonia concentration (Vol%)	Reaction pressure (MPa)	WHSV (mL g_{cat}^{-1} h^{-1})	Reference
1	$(H_3O)_2[(Mo_6Cl_8)Cl_6]\cdot 6H_2O$ (**1**) /MCM41	2.36	10.2(0.7)	0.241(0.018)	0.032	1.0	18000	This work
2	$(H_3O)_2[(Mo_6Cl_8)Cl_6]\cdot 6H_2O$ (**1**) /HZSM5	2.36	14.7(1.1)	0.348(0.025)	0.046	1.0	18000	This work
3	$(H_3O)_2[(Mo_6Cl_8)Cl_6]\cdot 6H_2O$ (**1**) /HY	2.36	20.5(0.7)	0.483(0.015)	0.065	1.0	18000	This work
4	$(H_3O)_2[(Mo_6Cl_8)Cl_6]\cdot 6H_2O$ (**1**) /HY	2.36	37.1(1.2)	0.876(0.028)	0.12	2.0	18000	This work
5	$Mo(\equiv CBu^t)(Np)_3/SiO_2$	2.0	6.8	0.136	0.027	2.0	12000	15
6	MoN_x/HZSM5	2.17	4.3	0.093	0.025	2.0	9000	16
7	MoC_x/HZSM5	2.17	4.5	0.099	0.026	2.0	9000	16
8	Fe industrial catalyst	>90[17]	<16[a]	14	0.31	0.9	36000	18
9	Ba-Ru/C	9.1	91.0[b]	8.2	1.1	0.9	18000	18
10	Ru/Ba-$Ca(NH_2)_2$	10	500[b]	50	3.4	0.9	36000	18
11	$Ru/La_{0.5}Pr_{0.5}O_{1.75}$_650red	5.0	1204[b]	60.2	2.0	1.0	72000	19
12	Ba_2RuH_6/MgO[c]	5.0	1440[b]	72	2.9	1.0	60000	20

[a] mmol g_{Fe}^{-1} h^{-1}.

[b] mmol g_{Ru}^{-1} h^{-1}.

[c] Reaction data at 375 °C.

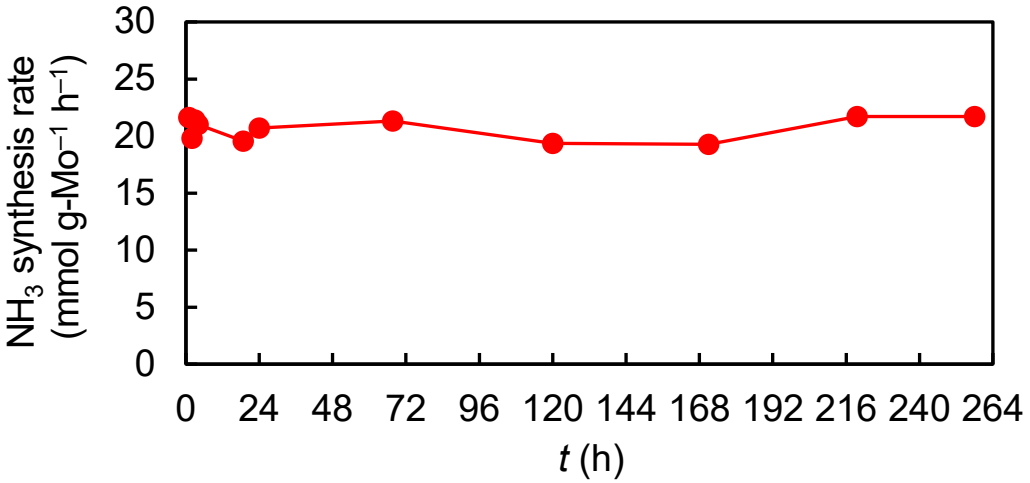

Fig. S14. Durability of ammonia synthesis activity at 400 °C and 1.0 MPa (absolute pressure), using $(H_3O)_2[(Mo_6Cl_8)Cl_6]\cdot 6H_2O$ (**1**)/HY as the precursor.

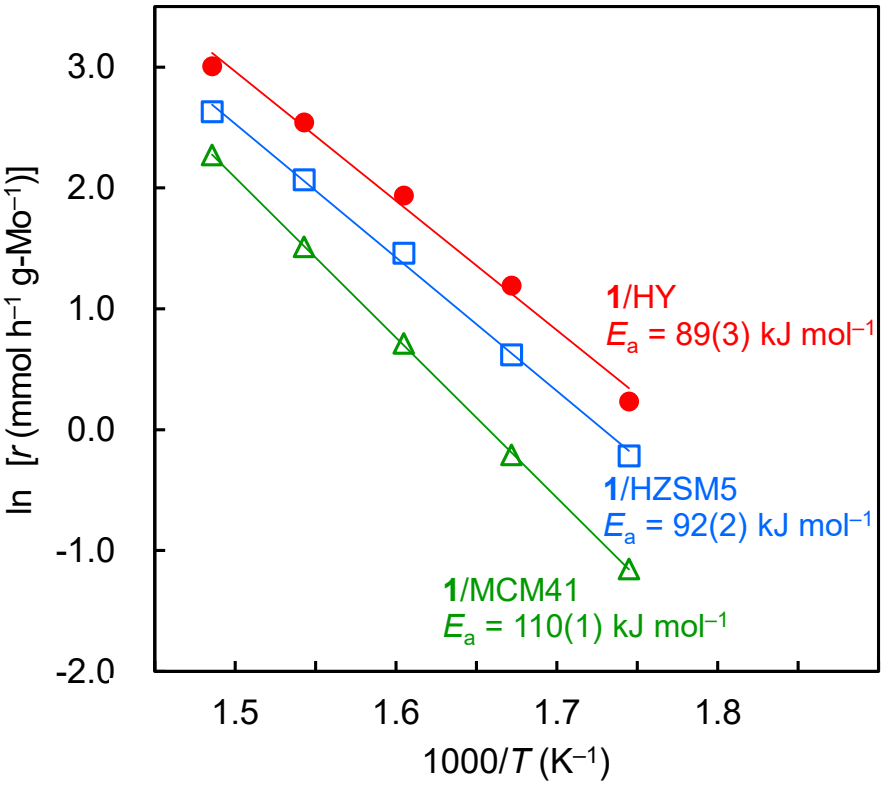

Fig. S15. Arrhenius plots for ammonia synthesis reactions at 1.0 MPa (absolute pressure), using supported $(H_3O)_2[(Mo_6Cl_8)Cl_6]\cdot 6H_2O$ (**1**) as the precursors. The experiments were performed at least three times, and the values in the parentheses are standard deviations.

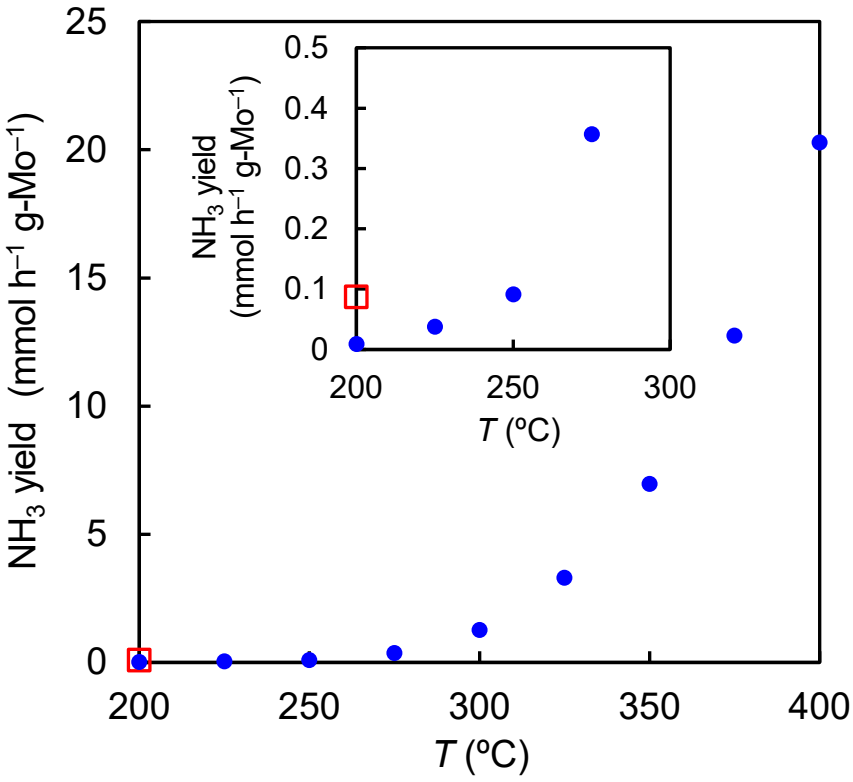

Fig. S16. Temperature dependence on ammonia synthesis activity at 1.0 MPa (absolute pressure), using $(H_3O)_2[(Mo_6Cl_8)Cl_6]\cdot 6H_2O$ (**1**)/HY as the precursor. The plot at 200 °C and 5.0 MPa (absolute pressure) is also shown as a red square.

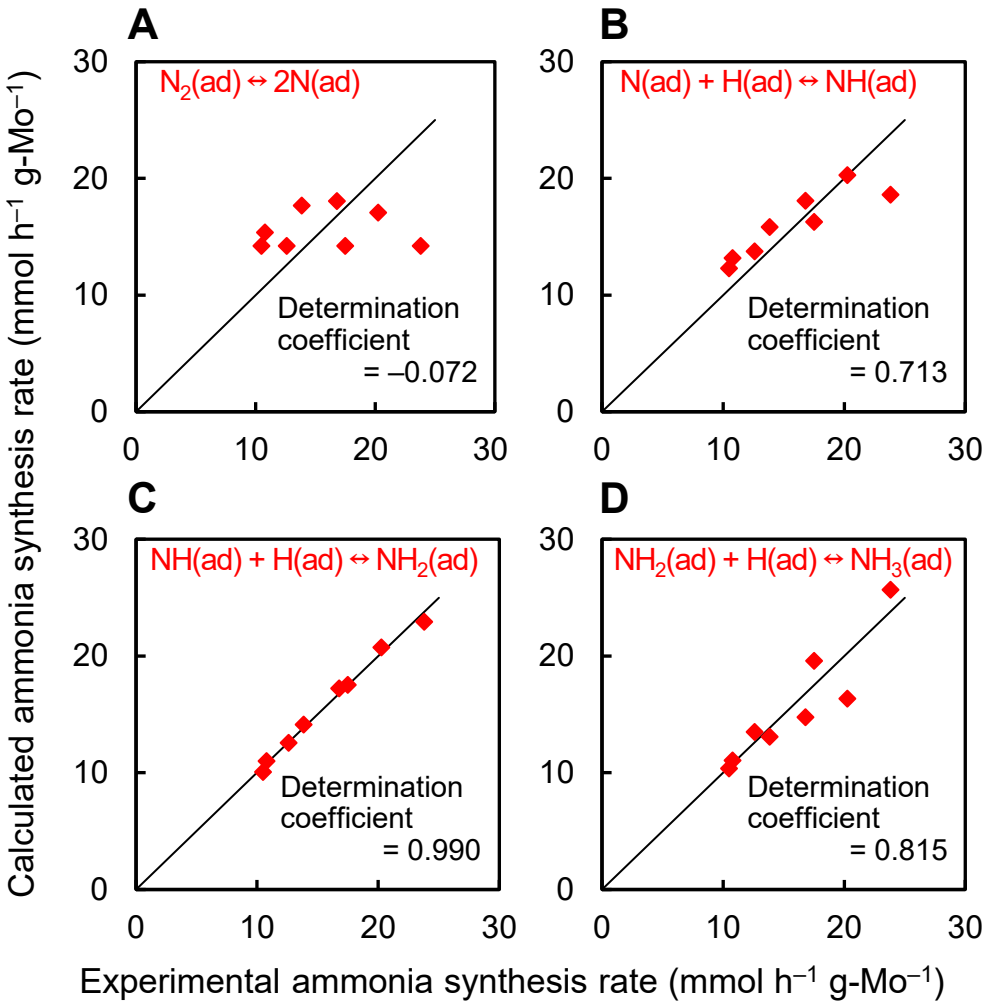

Fig. S17. Best-fit results for ammonia synthesis rate over HY-supported Mo metal cluster catalyst, assuming that RDS is (A) N_2 activation, (B) NH formation, (C) NH_2 formation, and (D) NH_3 formation.

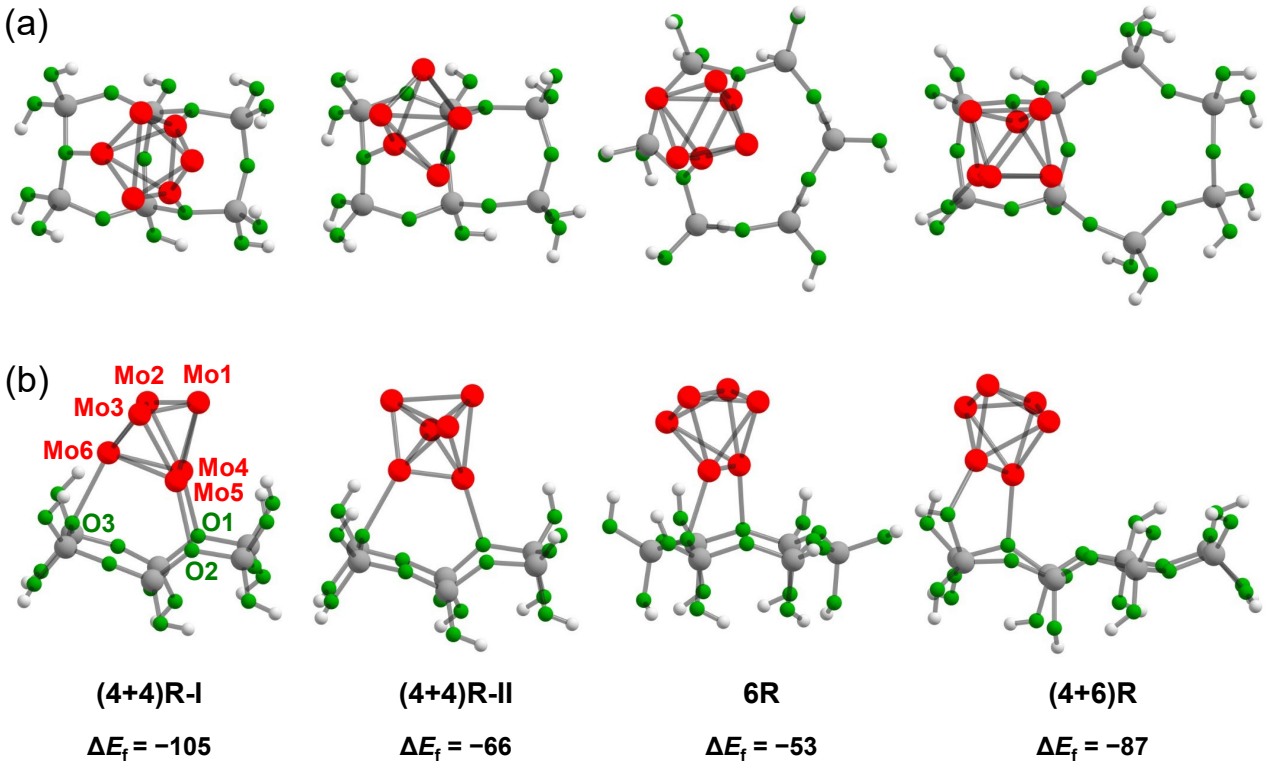

Fig. S18. Structure of Mo_6 accommodated on various local structure of Y-zeolite determined by DFT calculations: (a) top view (b) side view. (Red, Mo; green, O; gray, Si; white, H)

Table S6. Interatomic distances (in Å) of Mo_6@(4+4)R-I model.

	Distance / Å
Mo1−Mo2	2.30
Mo1−Mo3	2.29
Mo1−Mo4	2.77
Mo1−Mo5	2.75
Mo1−Mo6	3.41
Mo2−Mo3	2.81
Mo2−Mo4	2.52
Mo2−Mo5	3.53
Mo2−Mo6	2.35
Mo3−Mo4	3.56
Mo3−Mo5	2.54
Mo3−Mo6	2.35
Mo4−Mo5	2.19
Mo4−Mo6	2.67
Mo5−Mo6	2.66
Mo4−O1	2.37
Mo5−O2	2.36
Mo6−O3	2.63

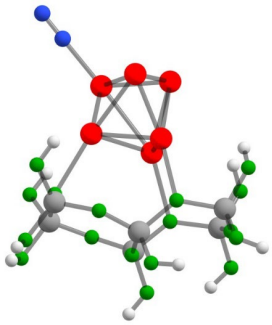

A1
ΔE_{ad} = −39

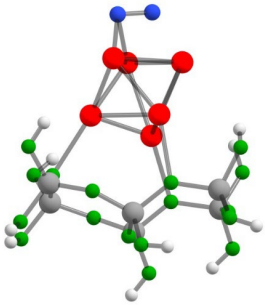

A2
ΔE_{ad} = 7

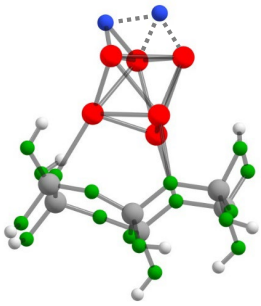

TS_{A2A3}
ΔE_{ad} = 126
ΔE_{act} = 119

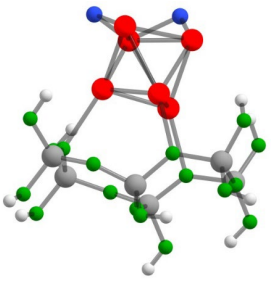

A3
ΔE_{ad} = −125

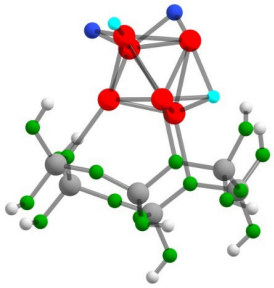

A4
ΔE_{ad} = −242

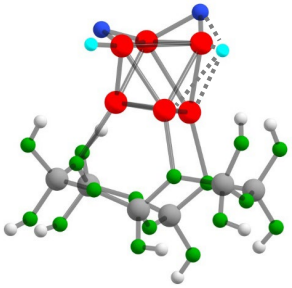

TS_{A4A5}
ΔE_{ad} = −106
ΔE_{act} = 136

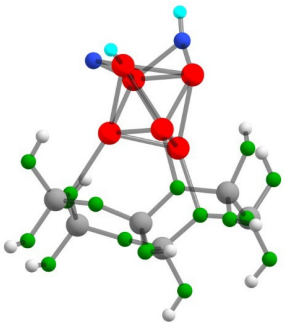

A5
ΔE_{ad} = −231

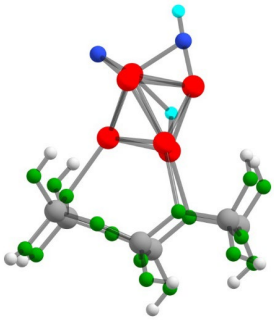

A5′
ΔE_{ad} = −172

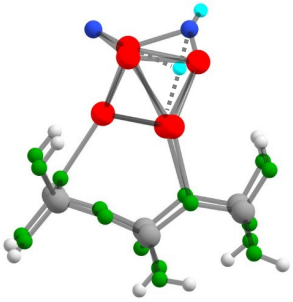

$TS_{A5'A6}$
ΔE_{ad} = −55
ΔE_{act} = 117

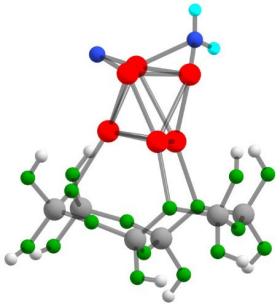

A6
ΔE_{ad} = −189

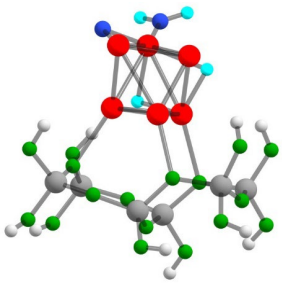

A7
ΔE_{ad} = −343

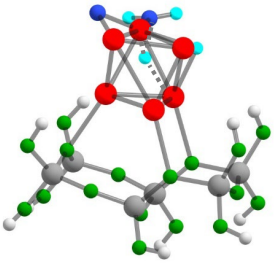

TS_{A7A8}
ΔE_{ad} = −181
ΔE_{act} = 162

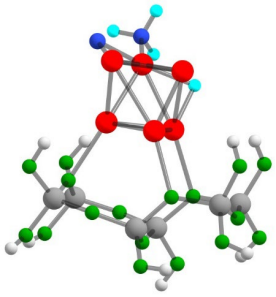

A8
ΔE_{ad} = −258

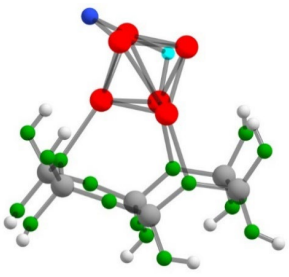

A9
ΔE_{ad} = −163

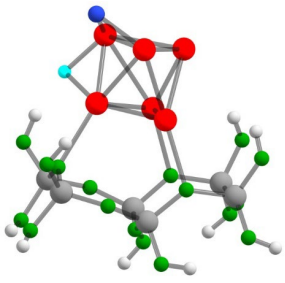

A9′
ΔE_{ad} = −104

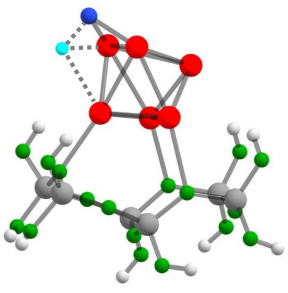

$TS_{A9'A10}$
ΔE_{ad} = 15
ΔE_{act} = 119

Fig. S19. (Continued)

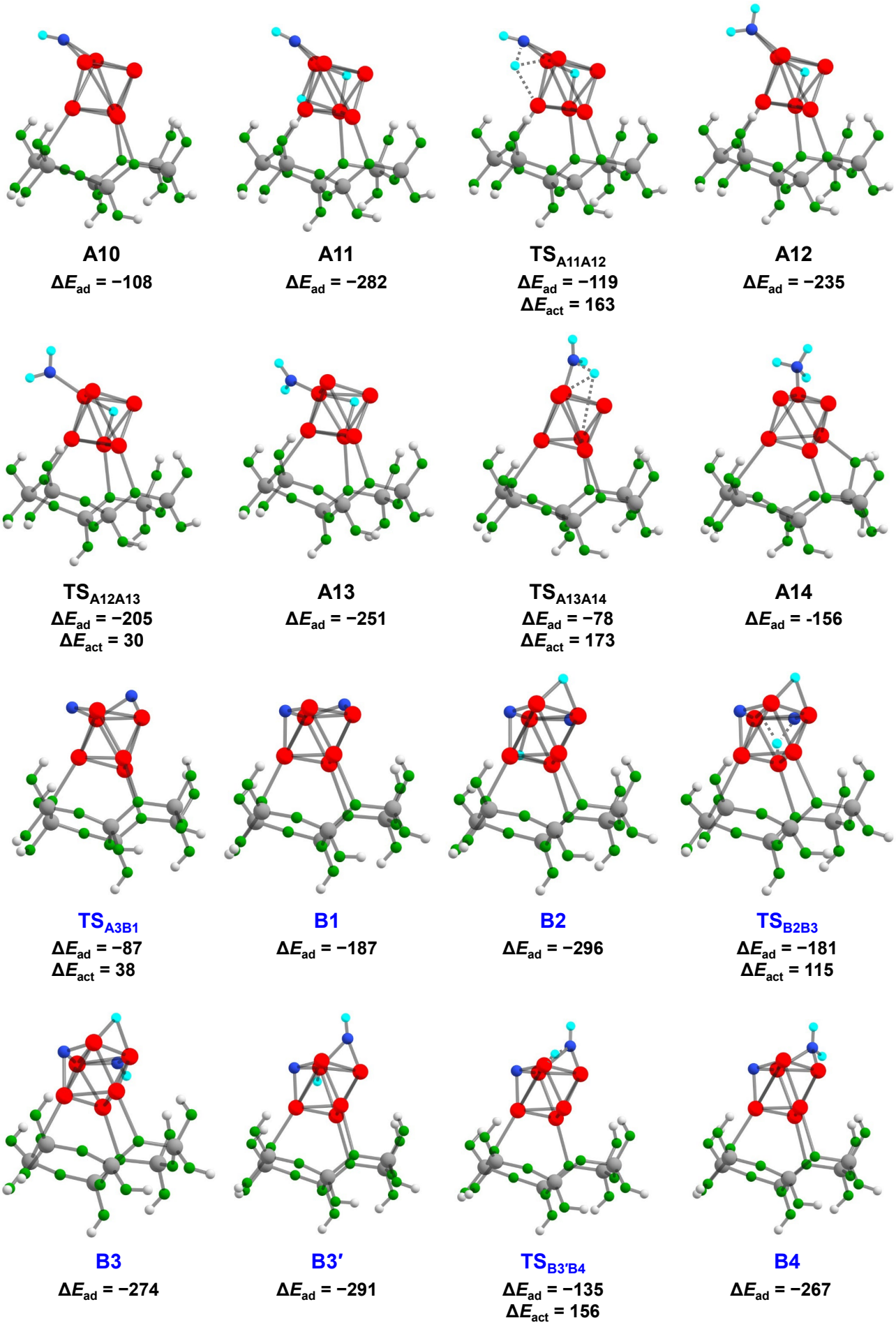

Fig. S19. (Continued)

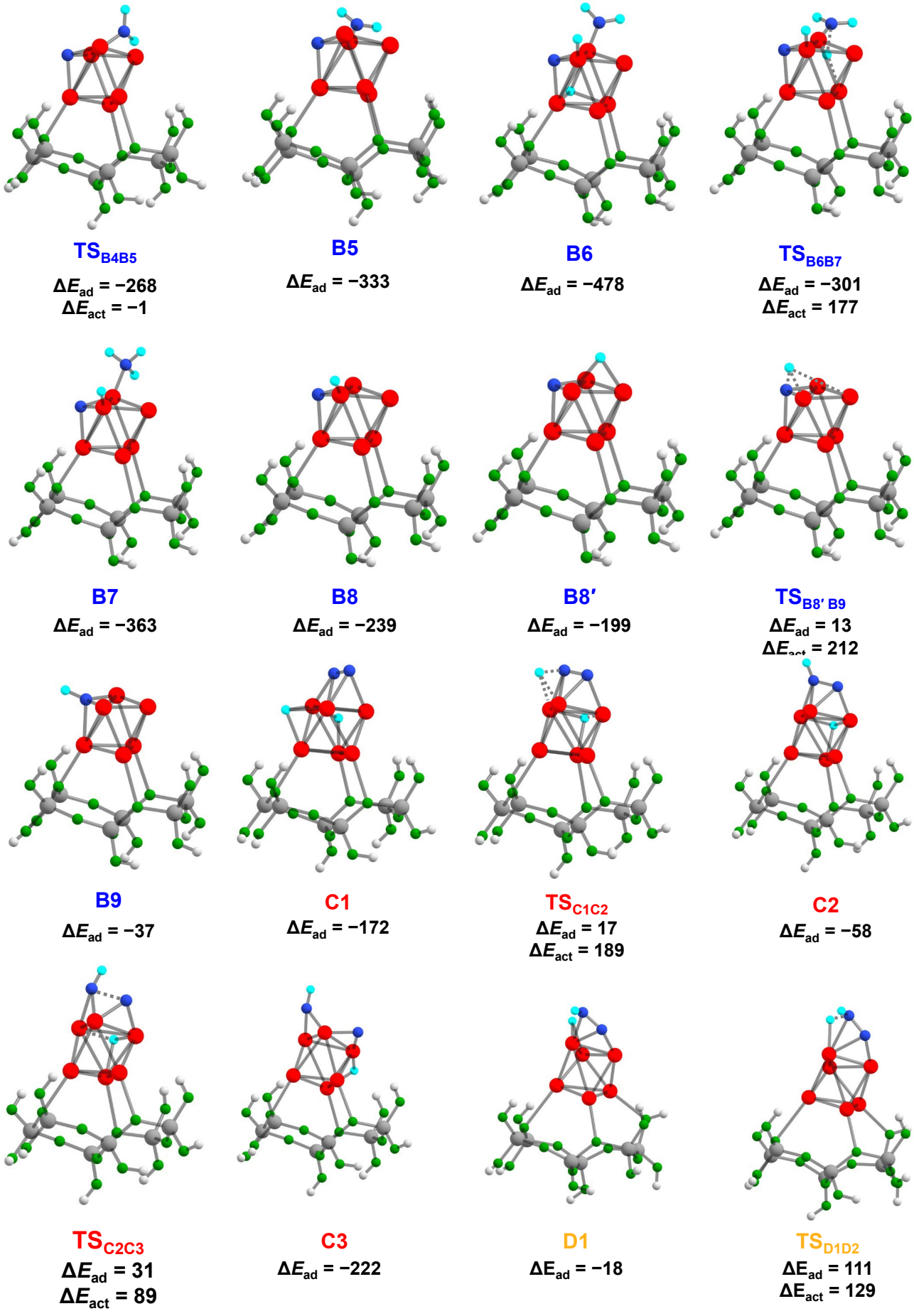

Fig. S19. (Continued)

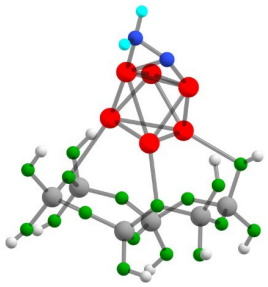

D2

ΔE_{ad} = 20

Fig. S19. Structure of various intermediates and transition states along the reaction pathway.

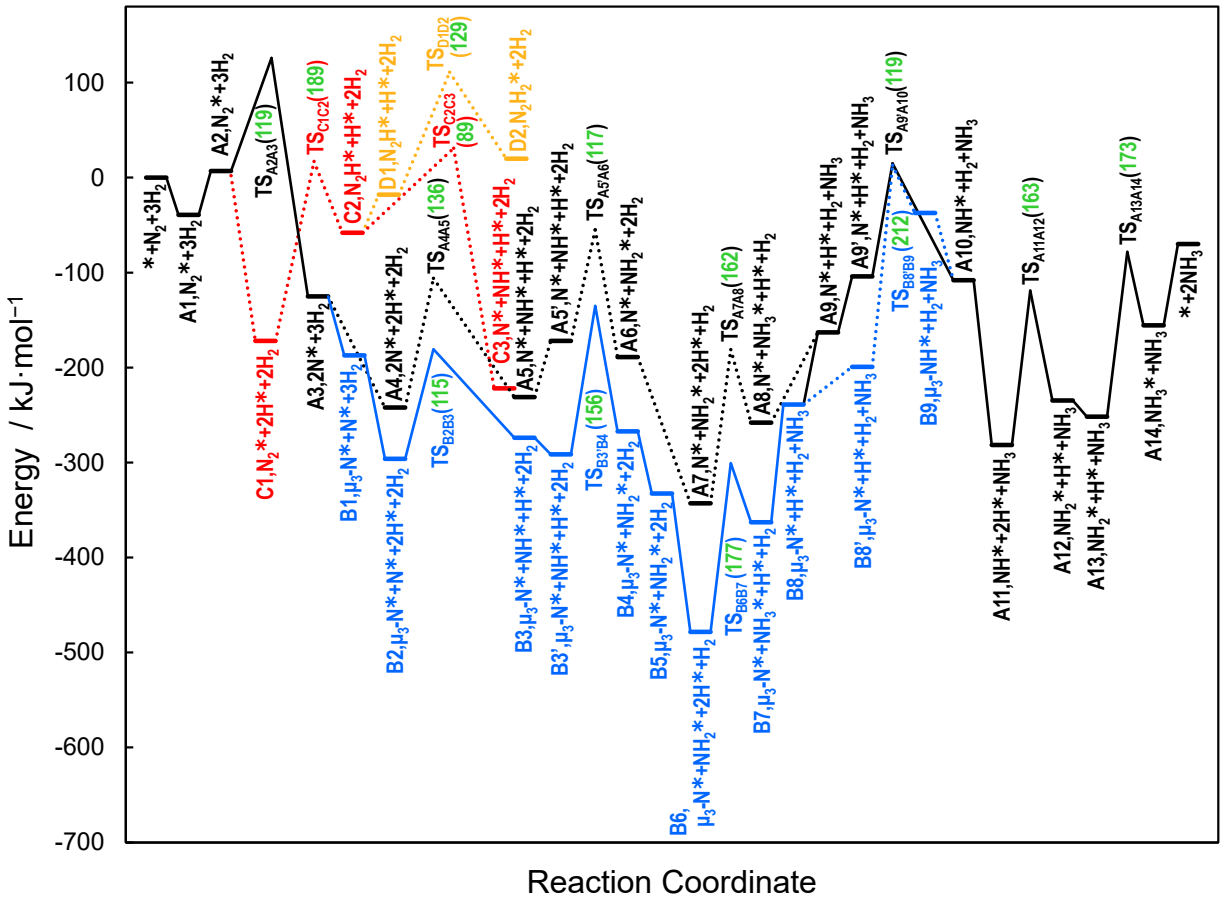

Fig. S20. Potential energy profiles of the dissociative mechanism (pathways A (black) and B (blue)) and the associative mechanism (pathway C (red) and D (orange)) for NH_3 synthesis on HY zeolite. Numbers in parentheses indicate the activation energy (in kJ mol^{-1}). The transition states with a low energy barrier (< 40 kJ mol^{-1}) are omitted for clarity, while all the intermediate structures and activation energies are given in Fig. S19. The transition states for H migration are not calculated since the barrier energies are much lower than those of N–N and N–H bond breaking/formation. The dominant reaction pathway determined by the microkinetic analysis follows not dashed but solid lines.

There are generally two accepted mechanisms for the NH_3 synthesis: the Langmuir–Hinshelwood (dissociative) mechanism in which the N–N bond dissociation precedes the N–H bond formation, and the Eley–Rideal/Mars–van Krevelen (associative) mechanism in which the N–H bond formation precedes the N–N bond dissociation.[21] As the dissociative mechanism, we computed two plausible pathways, in which, while one dissociated N is converted to NH_3, the other N takes a μ_2-bridging mode (pathway A) or a μ_3-bridging mode (pathway B). The pathway A is initiated by adsorption of N_2 molecule on a Mo atom in a terminal end-on mode (**A1**), followed by a configuration change of the Mo-bonded N into the μ_2-bridging adsorption mode (**A2**). Then, the N–N bond cleavage by participation of three Mo atoms takes place (**A3**). The first H_2 molecule is subsequently introduced as the dissociative adsorption (**A4**), followed by transfer of one H to the μ_2-bridging N to form a μ_2-bridging NH (**A5**). After migration of the remaining H atom (**A5**→**A5′**), the second H transfers to the NH to yield NH_2 (**A6**). Next, the second H_2 molecule is introduced as the dissociative adsorption

(**A7**). Then, the third H transfers to the NH_2 group affording a terminal NH_3 (**A8**), followed by a release of the first NH_3 molecule (**A9**). After the migration of the H atom (**A9→A9′**), the N atom accepts the fourth H atom to form a μ_2-bridging NH (**A10**). After the third introduction of the H_2 molecule (**A11**), the fifth H transfer gives a μ_2-bridging NH_2 (**A12**). Then, after the configuration change of the μ_2-bridging NH_2 to the terminal NH_2 (**A12→A13**), the sixth H transfer occurs to afford a terminal NH_3 (**A14**). Finally, the second NH_3 molecule is released. The pathway B starts by a configuration change of one N atom of **A3** from μ_2- to μ_3-bridging mode (**B1**), followed by similar mechanistic steps (from **B1** to **B9**) to those of the pathway A. The pathway B is terminated by configuration change of the μ_3-bridging N of **B9** to a μ_2-bridging mode again (**A10**).

As the associative mechanism, two pathways were proposed. In the pathway C, the first H_2 molecule is introduced without the N–N bond cleavage (**A2→C1**). Then, one H transfers to the N–N bond to yield a μ_2-bridging NNH with formation of the first N–H bond (**C2**), followed by N–N bond cleavage (**C3**). The distal pathway D is initiated by migration of the remaining H atom in **C2** to form μ_2-bridging H (**D1**), followed by its transfer to the NNH to afford NNH_2 group (**D2**).

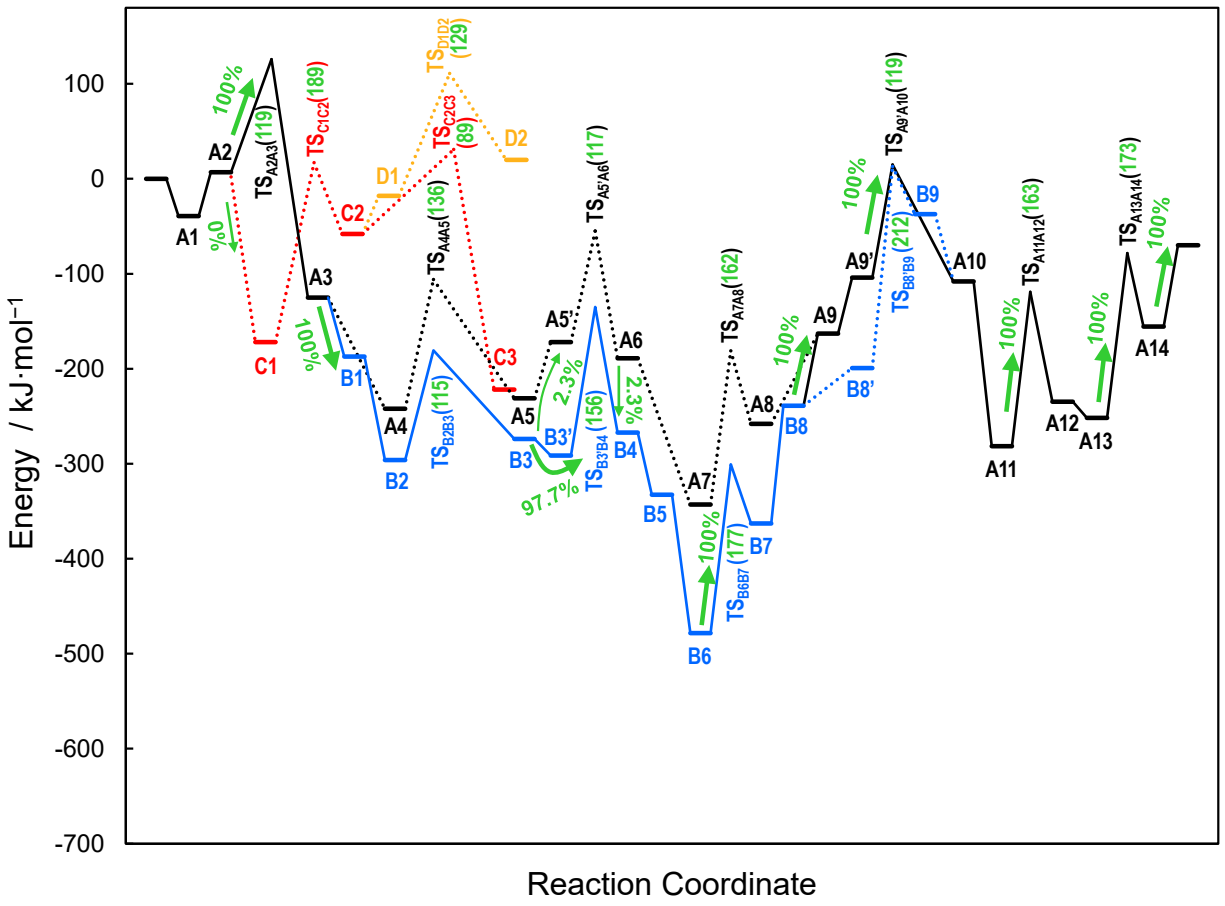

Fig. S21. Reaction flow determined by the microkinetic model. The dominant reaction pathway determined by this microkinetic analysis follows not dashed but solid lines.

The microkinetic analysis was performed for determination of the most plausible pathway. In this analysis, switches of the pathways between intermediates of the pathway A and the pathway B were also considered. As shown as a solid line, the dominant pathway follows the pathway A via **A1**, **A2**, and **A3**. Next, the pathway switches from the pathway A to the pathway B (**A3**→**B1**), and follows through the intermediates from **B2** to **B8**. Then, the pathway switches from the pathway B back to the pathway A (**B8**→**A9**), and follows through the rest of the intermediates from **A9′** to **A14**. The probabilities in the dominant pathway calculated by this microkinetic analysis are more than 98%. The contribution of the associative pathway (pathways C and D) is negligible, which is due to the higher barrier for the first N–H formation (189 kJ mol^{-1} via **TS$_{C1C2}$**).

Table S7. Elementary reaction steps involved in the microkinetic analysis. The site notation [A*, B*, C*] represents adsorption of A, B, and C on Mo_6. X(g) and X* represent X species in the gas phase and in adsorption state, respectively, and * denotes a free site. The adsorption state of N, such as μ_2- and μ_3-bridging, are distinguished by the notation (2) and (3), respectively.

	Reaction Type	**Elementary Step**
r1	N_2 adsorption	$N_2(g) + [*,*,*] \rightleftharpoons [N_2*,*,*]_D$
r2	N_2 adsorption	$N_2(g) + [*,*,*] \rightleftharpoons [N_2*,*,*]_A$
r3	H_2 adsorption	$H_2(g) + 2* \rightleftharpoons 2H*$
r4	N_2H formation	$[N_2*,*,*]_A + H* \rightleftharpoons [N_2H*,*,*] + *$
r5	N_2H dissociation	$[N_2H*,*,*] \rightleftharpoons [N(2)*,NH*,*]$
r6	N_2 dissociation	$[N_2*,*,*]_D \rightleftharpoons [N(2)*,N(2)*,*]$
r7	configuration change	$[N(2)*,N(2)*,*] \rightleftharpoons [N(3)*,N(2)*,*]$
r8	NH formation	$[N(3)*,N(2)*,*] + H* \rightleftharpoons [N(3)*,NH*,*] + *$
r9	NH formation	$[N(2)*,N(2)*,*] + H* \rightleftharpoons [N(2)*,NH*,*] + *$
r10	configuration change	$[N(2)*,NH*,*] \rightleftharpoons [N(3)*,NH*,*]$
r11	NH_2 formation	$[N(3)*,NH*,*] + H* \rightleftharpoons [N(3)*,NH_2*,*] + *$
r12	NH_2 formation	$[N(2)*,NH*,*] + H* \rightleftharpoons [N(2)*,NH_2*,*] + *$
r13	configuration change	$[N(2)*,NH_2*,*] \rightleftharpoons [N(3)*,NH_2*,*]$
r14	NH_3 formation	$[N(3)*,NH_2*,*] + H* \rightleftharpoons [N(3)*,NH_3*,*] + *$
r15	NH_3 formation	$[N(2)*,NH_2*,*] + H* \rightleftharpoons [N(2)*,NH_3*,*] + *$
r16	configuration change	$[N(2)*,NH_3*,*] \rightleftharpoons [N(3)*,NH_3*,*]$
r17	NH_3 adsorption	$NH_3(g) + [N(3)*,*,*] \rightleftharpoons [N(3)*,NH_3*,*]$
r18	NH_3 adsorption	$NH_3(g) + [N(2)*,*,*] \rightleftharpoons [N(2)*,NH_3*,*]$
r19	configuration change	$[N(2)*,*,*] \rightleftharpoons [N(3)*,*,*]$
r20	NH formation	$[N(3)*,*,*] + H* \rightleftharpoons [NH(3)*,*,*] + *$
r21	NH formation	$[N(2)*,*,*] + H* \rightleftharpoons [NH(2)*,*,*] + *$
r22	configuration change	$[NH(3)*,*,*] \rightleftharpoons [NH(2)*,*,*]$
r23	NH_2 formation	$[NH(2)*,*,*] + H* \rightleftharpoons [NH_2*,*,*] + *$
r24	NH_3 formation	$[NH_2*,*,*] + H* \rightleftharpoons [NH_3*,*,*] + *$
r25	NH_3 adsorption	$NH_3(g) + [*,*,*] \rightleftharpoons [NH_3*,*,*]$

References

1 (a) P. Nannelli and B. P. Block, 29. Molybdenum (II) halides, *Inorg. Synth.* 1970, **12**, 170–178; (b) D. N. T. Hay, J. A. Adams, J. Carpenter, S. L. DeVries, J. Domyancich, B. Dumser, S. Goldsmith, M. A. Kruse, A. Leone, F. Moussavi-Harami, J. A. O'Brien, J. R. Pfaffly, M. Sylves, P. Taravati, J. L. Thomas, B. Tiernan, L. Messerle, Facile reduction of early transition metal halides with nonconventional, mild reductants. 6. A new, lower-temperature, solid-state synthesis of the cluster hexamolybdenum dodecachloride Mo_6Cl_{12} from $MoC1_5$, via chloromolybdic acid, $(H_3O)_2[Mo_6(\mu_3\text{-}Cl)_8Cl_6]\cdot 6H_2O$, *Inorg. Chim, Acta* 2004, **357**, 644–648.

2 "Handbook of Corrosion Data", 2nd Edition, eds. B. D. Craig and D. S. Anderson, ASM International, Materials Park, OH, 1995. (1995). pp. 462–466.

3 (a) F. Rosowski, A. Hornung, O. Hinrichsen, D. Herein, M. Muhler and G. Ertl, Ruthenium catalysts for ammonia synthesis at high pressures: Preparation, characterization, and power-law kinetics, *Appl. Catal. A* 1997, **151**, 443–460; (b) M. Kitano, S. Kanbara, Y. Inoue, N. Kuganathan, P. V. Sushko, T. Yokoyama, M. Hara and H. Hosono, Electride support boosts nitrogen dissociation over ruthenium catalyst and shifts the bottleneck in ammonia synthesis, *Nat. Commun.* 2015, **6**, 6731.

4 R. Kojima and K. Aika, Cobalt molybdenum bimetallic nitride catalysts for ammonia synthesis. Part 2. Kinetic study, *Appl. Catal. A* 2001, **218**, 121–128.

5 W. Gao, S. feng, H. Yan, Q. Wang, H. Xie, L. Jiang, W. Zhang, Y. Guan, H. Wu, H. Cao, J. Guo and P. Chen, In situ formed Co from a Co–Mg–O solid solution synergizing with LiH for efficient ammonia synthesis, *Chem. Commun.* 2021, **57**, 8576–8579.

6 (a) G. Ertl, Primary steps in catalytic synthesis of ammonia, *J. Vac. Sci. Technol. A* 1983, **1**, 1247–1253; (b) O. Hinrichsen, F. Rosowski, M. Muhler and G. Ertl, The microkinetics of ammonia synthesis catalyzed by cesium-promoted supported ruthenium, *Chem. Eng. Sci.* 1996, **51**, 1683–1690; (c) S. Dahl, J. Sehested, C. J. H. Jacobsen, E. Tornqvist and I. Chorkendorff, Surface Science Based Microkinetic Analysis of Ammonia Synthesis over Ruthenium Catalysts, *J. Catal.* 2000, **192**, 391–399

7 T. Taguchi, T. Ozawa and H. Yashiro, REX2000: yet another XAFS analysis package, *Phys. Scr.* 2005, **T115**, 205–206.

8 K. Asakura, In *X-ray Absorption Fine Structure for Catalysts and Surfaces*; Y. Iwasawa, Ed.; World Scientific: Singapore, 1996; p. 33.

9 J. J. Rehr, R. C. Albers, Theoretical approaches to x-ray absorption fine structure, *Rev. Mod. Phys.* 2001, **72**, 621–654.

10 W. C. Hamilton, Significance Tests on the Crystallographic R Factor, *Acta Crystallogr.* 1965, **18**, 502–510.

11 V. Ortalan, A. Uzun, B. C. Gates and N. D. Browning, Direct imaging of single metal atoms and clusters in the pores of dealuminated HY zeolite, *Nat. Nanotech.* 2010, **5**, 506–510.

12 M. J. Frisch, G. W. Trucks, H. B. Schlegel, G. E. Scuseria, M. A. Robb, J. R. Cheeseman, G. Scalmani, V. Barone, G. A. Petersson, H. Nakatsuji, X. Li, M. Caricato, A. V. Marenich, J. Bloino, B. G. Janesko, R. Gomperts, B. Mennucci, H. P. Hratchian, J. V. Ortiz, A. F. Izmaylov, J. L.

Sonnenberg, D. Williams-Young, F. Ding, F. Lipparini, F. Egidi, J. Goings, B. Peng, A. Petrone, T. Henderson, D. Ranasinghe, V. G. Zakrzewski, J. Gao, N. Rega, G. Zheng, W. Liang, M. Hada, M. Ehara, K. Toyota, R. Fukuda, J. Hasegawa, M. Ishida, T. Nakajima, Y. Honda, O. Kitao, H. Nakai, T. Vreven, K. Throssell, J. A. Montgomery, Jr., J. E. Peralta, F. Ogliaro, M. J. Bearpark, J. J. Heyd, E. N. Brothers, K. N. Kudin, V. N. Staroverov, T. A. Keith, R. Kobayashi, J. Normand, K. Raghavachari, A. P. Rendell, J. C. Burant, S. S. Iyengar, J. Tomasi, M. Cossi, J. M. Millam, M. Klene, C. Adamo, R. Cammi, J. W. Ochterski, R. L. Martin, K. Morokuma, O. Farkas, J. B. Foresman and D. J. Fox, Gaussian 16, Revision C.01. Gaussian Inc.: Wallingford CT 2016.

13 I. A. Filot, Introduction to Microkinetic Modeling. Tech. Univ. Eindhoven 2018, 1–217.

14 (a) C. Deng, J. Zhang, L. Dong, M. Huang, B. Li, G. Jin, J. Gao, F. Zhang, M. Fan, L. Zhang and Y. Gong, The effect of positioning cations on acidity and stability of the framework structure of Y zeolite, *Sci. Rep.* 2016, **6**, 23382; (b) T. Iida, M. Shetty, K. Murugappan, Z. Wang, K. Ohara, T. Wakihara and Y. Román-Leshkov, Encapsulation of Molybdenum Carbide Nanoclusters inside Zeolite Micropores Enables Synergistic Bifunctional Catalysis for Anisole Hydrodeoxygenation, *ACS Catal.* 2017, **7**, 8147–8151.

15 L. M. Azofra, N. Morlanes, A. Poater, M. K. Samantaray, B. Vidjayacoumar, K. Albahily, L. Cavallo and J.-M. Basset, Single-Site Molybdenum on Solid Support Materials for Catalytic Hydrogenation of N_2-into-NH_3, *Angew. Chem. Int. Ed.* 2018, **57**, 15812–15816.

16 N. Liu, L. Nie, N. Xue, H. Dong, L. Peng, X. Guo and W. Ding, Catalytic Ammonia Synthesis over Mo Nitride/ZSM-5, *ChemCatChem* 2010, **2**, 167–174.

17 H. Hosono, M. Kitano, Advances in Materials and Applications of Inorganic Electrides, *Chem. Rev.* 2021, **121**, 3121–3185.

18 M. Kitano, Y. Inoue, M. Sasase, K. Kishida, Y. Kobayashi, K. Nishiyama, T. Tada, S. Kawamura, T. Yokoyama, M. Hara and H. Hosono, Self-organized Ruthenium–Barium Core–Shell Nanoparticles on a Mesoporous Calcium Amide Matrix for Efficient Low-Temperature Ammonia Synthesis, *Angew. Chem. Int. Ed.* 2018, **57**, 2648–2652.

19 Y. Ogura, K. Tsujimaru, K. Sato, S. Miyahara, T. Toriyama, T. Yamamoto, S, Matsumura, $Ru/La_{0.5}Pr_{0.5}O_{1.75}$ Catalyst for Low-Temperature Ammonia Synthesis, *ACS Sustainable Chem. Eng.* 2018, **6**, 17258−17266.

20 C. Liu, Q. Wang, J. Guo, T. Vegge, P. Chen, H. A. Hansen, Ba_2RuH_6 Forming a Complex Active Center for Non-dissociative Dinitrogen Activation and Ammonia Formation, *ACS Catal.* 2022, **12**, 4194–4202.

21 (a) C. D. Zeinalipour-Yazdi, J. S. Hargreaves and C. R. A. Catlow, Low-T Mechanisms of Ammonia Synthesis on Co_3Mo_3N, *J. Phys. Chem. C* 2018, **122**, 6078–6082; (b) T. Ye, S. Park, Y. Lu, J. Li, M. Sasase, M. Kitano, T. Tada and H. Hosono, Vacancy-enabled N_2 activation for ammonia synthesis on an Ni-loaded catalyst, *Nature* 2020, **583**, 391–395.